



# Inundation, runup and flow velocity of wavemaker generated bores on a planar beach

Ignacio Barranco<sup>1,2,†</sup> and Philip L.-F. Liu<sup>1,3,4,5</sup>

<sup>1</sup>Department of Civil and Environmental Engineering, National University of Singapore, Singapore 119077, Republic of Singapore

<sup>2</sup>HR Wallingford, Howbery Park, Wallingford OX10 8BA, UK

<sup>3</sup>School of Civil and Environmental Engineering, Cornell University, Hollister Hall, 220, College Ave, Ithaca, NY, USA

<sup>4</sup>Institute of Hydrological and Oceanic Sciences, National Central University, No. 300, Zhongda Rd, Zhongli District, Taoyuan City, Taiwan 320

<sup>5</sup>Department of Hydraulic and Ocean Engineering, National Cheng Kung University, No. 1, Dasyue Rd, East District, Tainan City, Taiwan 701

(Received 29 November 2021; revised 31 January 2023; accepted 31 January 2023)

Undulating and breaking bores are generated in the laboratory using a programmable long-stroke wavemaker. By changing the stroke length and the speed of the wavemaker, both non-decaying and decaying bores are generated and studied. Bore strength, height and duration are measured and compared with the solutions derived by using the method of characteristics, with excellent agreement. The measurements for inundation depth, runup height and flood duration are checked with the formulas presented in Barranco & Liu (*J. Fluid Mech.*, vol. 915, 2021). The comparisons show that the formulas are also accurate for the non-decaying bores generated by the wavemaker. The maximum inundation depth predicted by the formula for zero bore length at the beach toe agrees with the laboratory observations for decaying bores. Using a high-speed particle image velocimetry system, the ensemble-averaged velocities and fluctuating velocities under undulating bores and breaking bores are measured in constant water depth and in the vicinity of the still water shoreline. Detailed analyses of the velocity fields are presented and discussed. For the undulating bore a long quiescent flood duration is observed, while for the breaking bore the up-rush flow changes into down-rush flow almost linearly.

**Key words:** shallow water flows, wave breaking, coastal engineering

† Email address for correspondence: [i.barranco@u.nus.edu](mailto:i.barranco@u.nus.edu)

## 1. Introduction

Tidal bores and bore-like tsunami waves have been observed in coastal areas, where the bore front is either undulating or breaking (Shuto 1985; Simpson, Fisher & Wiles 2004; Chanson 2011; Takahashi & Tomita 2013). Historically, tsunami events have caused severe coastal flooding, beach erosion and infrastructure damage. Therefore, it is important to understand the fundamentals of the inundation and runup processes associated with undulating and breaking bores, and non-decaying and decaying bores on a slope. The decaying bore is defined as a bore with zero bore length whose bore strength and bore height decrease as it propagates.

The history of bore research, both theoretical and experimental, is long. A review on the subject has been provided by Barranco (2021) and will not be repeated here. Only the literature most relevant to the present study are highlighted herein. Many laboratory bore experiments have been reported. The most common method to generate a bore is to use a dam-break system, in which a volume of water, stored in a reservoir, is suddenly released by instantaneously lifting the reservoir gate. In most of existing experiments, only the free surface profiles in constant water depth (Stansby, Chegini & Barnes 1998) and the shoreline motions associated with bores (Yeh, Ghazali & Marton 1989) are measured. Barranco & Liu (2021) studied the inundation produced by bores of different strengths and lengths, which were generated by using various reservoir lengths, and highlighted the importance of the bore length on inundation. They provided analytical relations to calculate the length of bores reaching the beach toe. In addition, they proposed predictive formulas, based on numerical results, for the maximum inundation depth, runup height and flood duration as a function of bore strength and bore length at beach toe.

Bores can also be generated in the laboratory by using a wavemaker system, where a vertical paddle is pushed horizontally to displace the water in front of it. Using such a bore generation mechanism, Miller (1968) studied bore runup on slopes with different roughness and observed that bores with strength  $F < 1.25$  (the bore strength will be defined in §3) presented an undulating bore front, while bores with strength  $F > 1.55$  exhibited a breaking front. Based on the laboratory results, Miller provided the relations for the maximum runup as functions of bore height, slope and roughness, which are different for undulating bores and breaking bores (i.e. for different ranges of bore strength). Miller's findings are in contrast to the runup formula given in Barranco & Liu (2021), which indicates that the bore runup is independent of the bore type. Pujara *et al.* (2020) used piston-type wavemakers to generate transient waves of elevation, including solitary waves and short undulating bores. Ultrasonic wave gauges and acoustic Doppler velocimeters were used to measure the swash flows on a beach of composited slopes. Their results point out that the shoreline trajectory and, therefore, the maximum runup, depend on the wave acceleration phase. They also show that waves generated with the same stroke produced similar down-rush flows, independent of wave height. Based on these observations, Pujara *et al.* (2020) concluded that the wave-integrated volume flux was the parameter with greater influence on the down-rush flow.

In recent years, the particle image velocimetry (PIV) technique has been used to measure flow velocities in water columns in constant depth and swash regions under laboratory generated undulating bores (Lin *et al.* 2019, 2020*a,b*) and breaking bores (Hornung, Willert & Turner 1995; Barnes *et al.* 2009; O'Donoghue, Pokrajac & Hondebrink 2010; Kikkert *et al.* 2012), respectively. Employing a dam-break system, Lin *et al.* (2020*a*) studied undulating bores on a horizontal bed with different reservoir lengths. They measured the free surface elevations and horizontal velocities, and demonstrated the applicability of the Froude number scaling. The maximum and minimum values for the

horizontal velocities were observed in Lin *et al.* (2020*b*) at the crest and trough phases, respectively, while the vertical velocity profiles are almost zero. On the other hand, the maximum and minimum vertical velocities are observed at the zero-up/down-crossing phases. In an earlier study, Lin *et al.* (2019) reported the flow velocities under an undulating bore over a 1/20 slope, whose leading undulation broke on the slope. The field of view (FOV) of their study was located in the vicinity of the still water shoreline. The broken bore showed positive (on-shore) fluctuating velocities during the leading undulations. They were followed by a continuous decrease on the horizontal flow velocities until the maximum inundation was reached, indicating that the swash flow changed the direction. During the rundown the magnitude of the offshore flow velocities increased as the water depth decreased.

Using PIV, Hornung *et al.* (1995) measured flow velocities under a dam-break generated breaking bore in a constant depth. They observed large horizontal velocities near the breaking bore front, which decreased to a constant in the water column. They also discussed vorticity measurements and their generation due to unsteady and air entrainment effects. O'Donoghue *et al.* (2010) measured the horizontal velocity and turbulence fields during the swash flow produced by a strong breaking bore over smooth and rough slopes. They observed that turbulent velocities were higher during the up-rush than during the backwash, especially for rough slopes, and that the turbulent velocity decayed very rapidly as the flow decelerated. The turbulent velocities during the up-rush are associated with turbulence advected with the bore front. During the backwash, high velocities generate turbulence from the bed. In the smooth slope case, turbulent velocities were observed to be close to depth uniform, while in rough slopes they observed vertical structures with larger turbulent velocities towards the bed, during both the up-rush and backwash. In addition, they calculated the bed shear stresses from the horizontal velocity measurements near the bed and compared with the measurements in Barnes & Baldock (2006) with good agreement during the up-rush phase. The bore runup measured in the smooth slope agrees well with the formula shown in Barranco & Liu (2021). However, Barranco & Liu also pointed out that the bores generated in Barnes & Baldock (2006) and O'Donoghue *et al.* (2010) were too short to reach the maximum inundation depth of the flood plateau.

While many articles have reported results for bores and their corresponding swash flows, generated by a dam-break system, there are only few studies on bores and the associated inundation processes, generated by a wavemaker system. Therefore, the first objective of this paper is to check if the predictive formulas for runup and inundation, presented in Barranco & Liu (2021) for dam-break generated bores, are applicable for the inundation produced by wavemaker generated bores. Wavemaker generated bores are described in terms of their bore strength and bore length at the time they reach the toe of the slope, following the methodology developed in Barranco & Liu (2021). Decaying bores are also studied herein. This is the first time that decaying bores and their decay rate have been investigated in the laboratory. The inundation produced by non-decaying and decaying bores is analysed and compared with the Barranco & Liu (2021) formulas.

The second objective of this paper is to investigate the velocity field in the constant depth and the swash regions, produced by an undulating bore (UB) and a breaking bore (BB). A high-speed PIV (HSPIV) system will be employed to measure the velocities in the water column. The velocity measurements are decomposed into the ensemble-averaged velocity and fluctuating velocity components. To the best of our knowledge, the flow velocity measurements for the UB case on the slope are the first reported laboratory data, showing a flood plateau with quiescent flow produced by a very long bore. Fluctuating velocity components, representing a new data set, are also analysed in both constant water depth and slope regions.

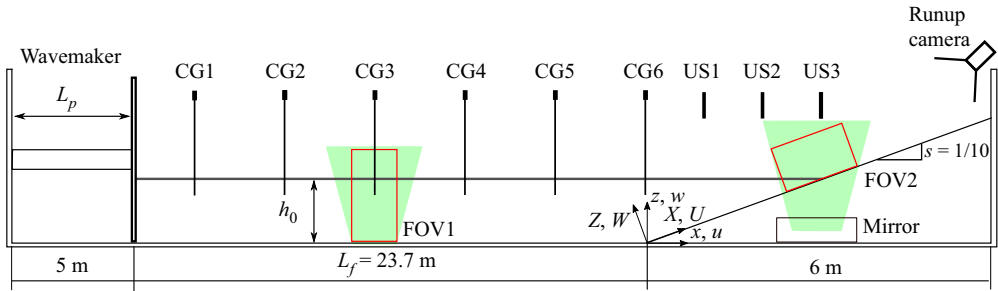


Figure 1. A sketch of the wavemaker and the experimental set-up (not to scale). Red areas represent HSPIV FOVs. The maximum wavemaker stroke is  $L_p = 5$  m.

This paper is structured as follows. In the next section the laboratory set-up and methodology are introduced. In § 3, general definitions discussed in the literature for bores are summarized and laboratory results of the bore evolution in a constant depth are presented. In § 4, inundation depths, runup heights and flood duration measurements are presented and compared with predictive relations from the literature. In §§ 5 and 6 flow fields for an UB and a BB are measured in the constant depth and slope regions, respectively. These measurements are analysed and contrasted with theoretical solutions and former observations in the literature. Finally, concluding remarks are provided in § 7.

## 2. Laboratory set-up

Laboratory experiments have been carried out in the wave flume in the Hydraulic Laboratory at the National University of Singapore (NUS). The wave flume is 36 m long, 0.9 m wide and 0.9 m high. At one end of the flume a 6 m long glass beach (1 : 10 slope) is installed. The wave flume is equipped with a piston-type wavemaker with a 5 m stroke (figure 1). The closest distance between the wavemaker position and the beach toe is 28.7 m. The wavemaker has a maximum speed of  $2.5 \text{ m s}^{-1}$  and a maximum acceleration (and deceleration) of  $3.5 \text{ m s}^{-2}$ , which is driven by two parallel linear actuators controlled by an AC Servo Motor. A flexible rubber seal has been installed along the edges of the wave paddle to minimize water leaks. The wave flume is equipped with six capacitance wave gauges (CG), three ultrasound sensors (US), one full HD camera and a HSPIV system. The capacitance gauges are used to measure the surface elevations of bores in the constant water depth region. The non-intrusive ultrasound sensors are deployed above the slope. A full HD camera is employed to record the runup on the slope.

The camera used in the HSPIV system is a Phantom LAB340, which has a 12-bit dynamic range and is capable of filming at 800 fps at maximum resolution ( $2560 \times 1600$ ). The frame rate used in the experiments is 500 fps. The camera lens is a Tokina AT-X PRO Macro 100 mm f2.8D, providing a high image quality with negligible image distortion. The light source for illuminating the particles in the water is a continuous 8W 532 nm diode-pumped solid-state laser, equipped with an optical sheet unit. Finally, the seeding particles for HSPIV imaging are hollow glass spheres with  $10 \mu\text{m}$  mean diameter,  $1100 \text{ kg m}^{-3}$  density, 1.5 refractive index and a terminal settling velocity of  $7.9 \times 10^{-10} \text{ m s}^{-1}$ , which is much smaller than the range of velocities to be measured in this study.

As shown in figure 1, the HSPIV system is installed at two locations with two FOVs; FOV1 is in the constant water depth region and FOV2 is in the vicinity of still

Configuration	CG1	CG2	CG3	CG4	CG5	CG6	US1	US2	US3
1	-21.01	-20.01	-10.95	-9.96	-1	0	0.65	1.4	2.15
2	-21.29	-7.63	-2.22	0	—	—	0.91	1.73	2.28
3	-21.29	-9.87	-2.22	0	—	—	—	—	—

Table 1. Sensor locations in metres with the origin at the beach toe ( $x = 0$ ). Configuration 1 is the set-up without HSPIV measurements, configurations 2 and 3 are for two HSPIV measurements.

water shoreline. Also, FOV1 is illuminated by directing the laser beam upwards from below the glass bottom along the centreline of the flume. To illuminate FOV2, a mirror is placed on the wave flume bottom underneath the glass slope. The mirror forms a  $45^\circ$  angle to the flume bottom, re-directing the laser fan to the vertical direction, parallel to the flume walls, at 0.153 m from the glass sidewall through which the high-speed camera records. Because only one HSPIV system is available, the same experimental conditions are repeated to cover both FOV measurements.

PIVlab Thielicke & Stamhuis (2014) is employed to calculate flow velocities. For each case, images are pre-processed using a contrast limited adaptive histogram equalization filter with 20 px windows size and a high-pass filter with 15 px kernel size. Velocities are calculated employing a fast Fourier transform algorithm. The analysis starts with an initial interrogation window of  $128 \times 128$  px and has two passes before reaching the final interrogation window size of  $32 \times 32$  px. All the passes have a 50% overlapping step, giving a final resolution of  $16 \times 16$  px. Finally, a local median filter is applied to reject outliers with normalized fluctuations larger than  $5 \text{ px f}^{-1}$  and estimated noise level  $0.1 \text{ px f}^{-1}$  (Westerweel & Scarano 2005). The rejected vectors are then replaced by interpolated data. For each bore generation condition, 10 repetitions are made for HSPIV measurements, yielding ensemble-averaged velocity and fluctuating velocity fields.

When HSPIV measurements are not performed, six CGs are installed in the constant depth region and three USs in the slope region; the location of these sensors is summarized in table 1 (configuration 1). On the other hand, when HSPIV measurements are conducted, only four CGs are placed in the constant water depth region with two different configurations (see table 1). Configuration 2 corresponds to the case when the HSPIV is installed at FOV1 and configuration 3 is used for the case with the HSPIV positioned at FOV2. Capacitance gauges 1, 3 and 4 are placed at the same locations for both configurations. Finally, the maximum runup heights are not measured when the HSPIV system is at FOV2.

### 3. Bore generation and propagation in constant depth

In the laboratory, bores can be generated by pushing a wavemaker (a vertical paddle) over a distance  $L_p$  (stroke) with a constant velocity,  $u_b$ , in the still water depth,  $h_0$ . The generated bores can be characterized by the speed of the bore front,  $U_b$ , the flow velocity behind the front,  $u_b$ , and the bore height,  $h_b$ . Defining the bore strength as

$$F = \frac{U_b}{c_0}, \tag{3.1}$$

the following bore relations have been established based on the nonlinear shallow water equations (Stoker 1957; Liggett 1994) as:

$$\frac{u_b}{c_0} = F \frac{\sqrt{1 + 8F^2} - 3}{\sqrt{1 + 8F^2} - 1}, \tag{3.2}$$

$$\frac{h_b}{h_0} = \left(\frac{c_b}{c_0}\right)^2 = \frac{1}{2}(\sqrt{1 + 8F^2} - 1), \tag{3.3}$$

where  $c_b = \sqrt{gh_b}$  is the bore celerity,  $c_0 = \sqrt{gh_0}$  is the long-wave celerity for undisturbed water depth  $h_0$  and  $g$  is the gravitational acceleration,  $9.81 \text{ m s}^{-1}$ . To generate a bore, the bore strength is first specified for a still water depth  $h_0$ . Equation (3.2) is then used to determine the wavemaker speed,  $u_b$ . The descriptions for bore generation using a wavemaker can be found in the literature (Stoker 1957) and some of the bore characteristics are defined in Appendix A for later use. Here, only the effective period of a bore at a given location  $x_t$

$$T_{bt} = \frac{L_p}{u_b} + \frac{x_t}{u_b + c_b} - \frac{L_p + x_t}{U_b}, \tag{3.4}$$

and the relation for calculating the effective bore length at the beach toe

$$L_b = L_f \left(1 - \frac{u_b + c_b}{F_{in}c_0}\right) + L_p \left(\frac{u_b + c_b}{c_0}\right) \left(\frac{c_0}{u_b} - \frac{1}{F_{in}}\right), \tag{3.5}$$

are highlighted, where  $F_{in}$  is the input bore strength,  $U_b/c_0$ ,  $u_b/c_0$  and  $c_b/c_0$  can be expressed in terms of  $F_{in}$  as given in (3.1), (3.2) and (3.3), respectively, and  $L_f$  is the distance from the stopping position of the wave paddle to the beach toe. Equation (3.5) can also be used to determine the necessary stroke,  $L_p$ , to generate a bore that will reach the beach toe with a targeted effective bore length and bore strength.

In the present experiments, the range of input bore strengths is  $1.1 \leq F_{in} \leq 1.9$ , which includes UBs, undulating-breaking bores (UBBs) and BBs. The initial position of the wavemaker is specified according to the required stroke,  $x_0 = -(23.7 \text{ m} + L_p)$ , so that the wavemaker stops at the same location for all experiments (see figure 1). The wavemaker accelerates from the initial position to the desired velocity,  $u_b$ , with an acceleration of  $3.5 \text{ m s}^{-2}$ , and towards the end of wavemaker movement it decelerates at  $3.5 \text{ m s}^{-2}$  until it stops. Three different water depths are used in the experiments. When the HSPIV data are not taken, the still water depth is kept at  $h_0 = 0.15 \text{ m}$  and four wavemaker stroke lengths,  $L_p = 2 \text{ m}$ ,  $3 \text{ m}$ ,  $4 \text{ m}$  and  $5 \text{ m}$ , are employed. On the other hand, when HSPIV measurements are conducted, two conditions are used:  $h_0 = 0.24 \text{ m}$  with  $F_{in} = 1.1$  for generating UBs, and  $h_0 = 0.18 \text{ m}$  with  $F_{in} = 1.6$  for BBs. In both HSPIV experiments the maximum stroke length is  $L_p = 5 \text{ m}$ . The same experiments are repeated 3 times when HSPIV are not conducted, while 10 repetitions are made for each HSPIV experimental condition and configuration. The experimental conditions are summarized in table 2.

The time histories of free surface elevations at CG1 and CG4 (their locations can be found in table 1) for UBs ( $F_{in} = 1.1$ ), UBBs ( $F_{in} = 1.4$ ) and BBs ( $F_{in} = 1.6$ ) are plotted in figures 2, 3 and 4, respectively. For each bore strength, the free surface elevations corresponding to four different wavemaker strokes,  $L_p$ , are also plotted. The free surface profiles are synchronized at their arrival times at CG1. The arrival time of the bore front (denoted by square) is defined as the moment when the dimensionless free surface elevation becomes larger than 0.05 (i.e.  $\eta/h_0 > 0.05$ , see figures 2, 3 and 4). The same

Input strength ( $F_{in}$ )	1.1*	1.2	1.3	1.4	1.5	1.6*	1.7	1.8	1.9
Wavemaker speed ( $u_b/c_0$ )	0.130	0.254	0.375	0.492	0.607	0.720	0.831	0.941	1.049

Table 2. Dimensionless wavemaker speed ( $u_b/c_0$ ) based on the target input bore strength ( $F_{in}$ ). Here, “\*” denotes the HSPIV measurements, in which  $h_0 = 0.24$  m for  $F_{in} = 1.1$  (UB), and  $h_0 = 0.18$  m for  $F_{in} = 1.6$  (BB). In both cases  $L_p = 5$  m. For the cases without HSPIV measurements the still water depth is  $h_0 = 0.15$  m with four wavemaker strokes,  $L_p = 2, 3, 4$  and  $5$  m.

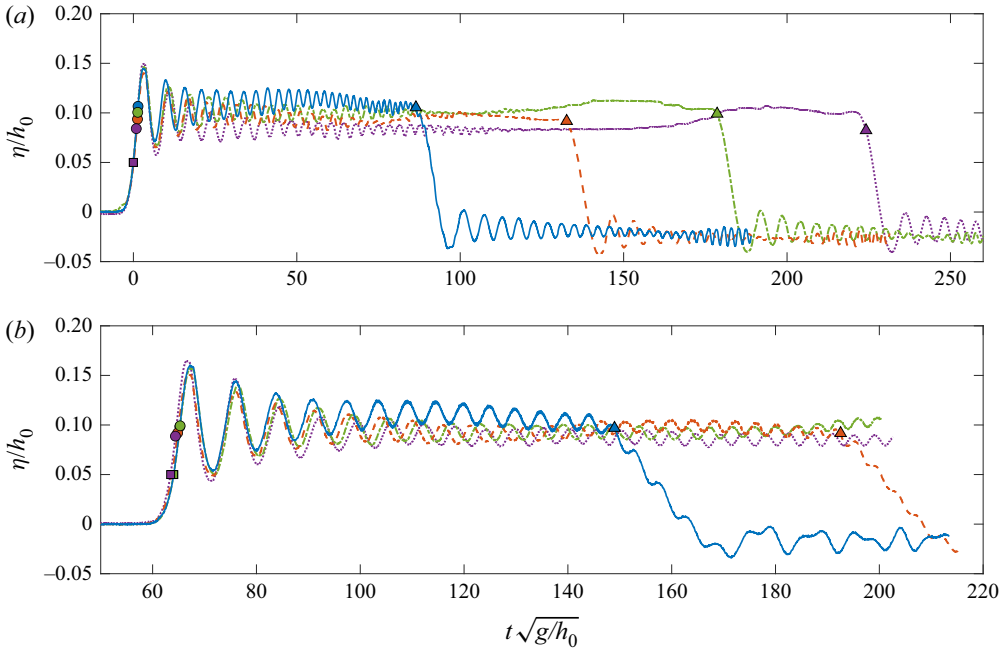


Figure 2. Time histories of dimensionless free surface elevations for UBs with  $F_{in} = 1.1$  at: (a) CG1 and (b) CG4. Results for  $L_p/h_0 = 13.33$  are plotted in solid blue line;  $L_p/h_0 = 20$  in dashed orange line;  $L_p/h_0 = 26.67$  in dashed-dotted green line; and  $L_p/h_0 = 33.33$  in dotted purple line. Squares represent the arrival of the bore front, triangles the beginning of the tail and circles the first measurement with bore height equal to or larger than the bore height at the beginning of the bore tail.

definition is applied to the measurements at the six capacitance gauges. The beginning of the bore tail (triangle) has also been identified for all cases (see figures 2, 3 and 4). The method for identifying the beginning of the bore tail is the same as that employed in Barranco & Liu (2021) and is generally robust for long bores. However, for short bores (e.g.  $L_p/h_0 = 13.33$ ), larger uncertainties exist because of the presence of undulations in the bore tail. To reduce the uncertainty, the method is modified slightly by taking only the data where  $\eta/h_0 > 0.4(\eta_{max}/h_0)$  into consideration for bore strength  $F < 1.35$ , where  $\eta_{max}/h_0$  is the maximum dimensionless surface height measured in each case and at each gauge. For bore strength  $F \geq 1.35$ , the undulations are smaller, and the minimum height limit is set at  $0.75(\eta_{max}/h_0)$ . More details can be found in the supplementary material available at <https://doi.org/10.1017/jfm.2023.116>.

The bore heights and periods have been measured at gauges CG1 to CG4, and their definitions are the same as those defined in Barranco & Liu (2021). Using a longer stroke, the generated bore duration lasts longer before forming a bore tail. The bore duration

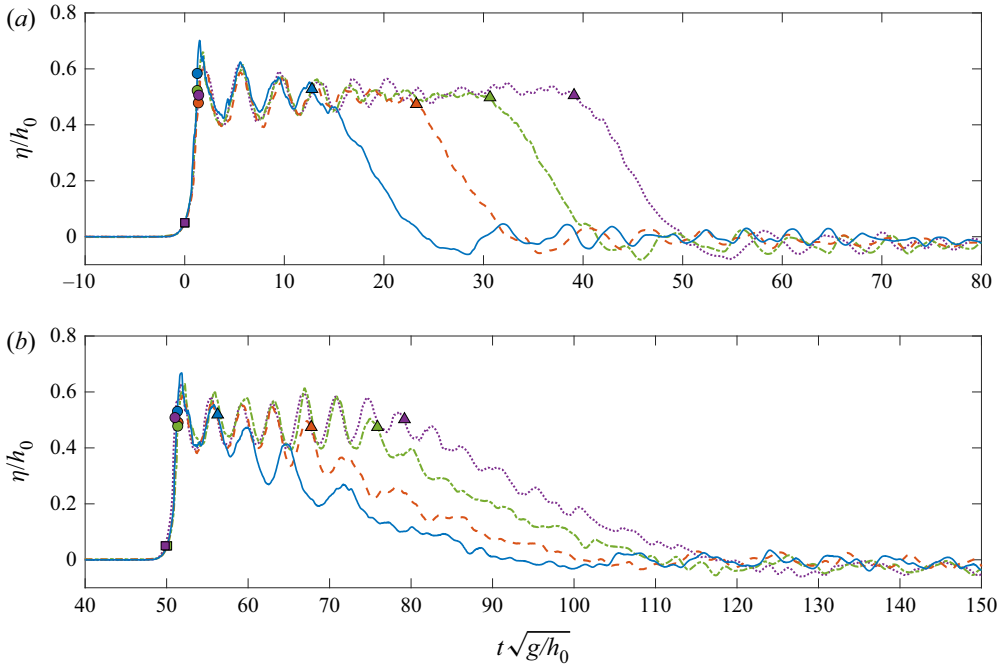


Figure 3. Time histories of dimensionless free surface elevations for UBBs with  $F_{in} = 1.4$  at: (a) CG1 and (b) CG4. For the remainder of the caption see figure 2.

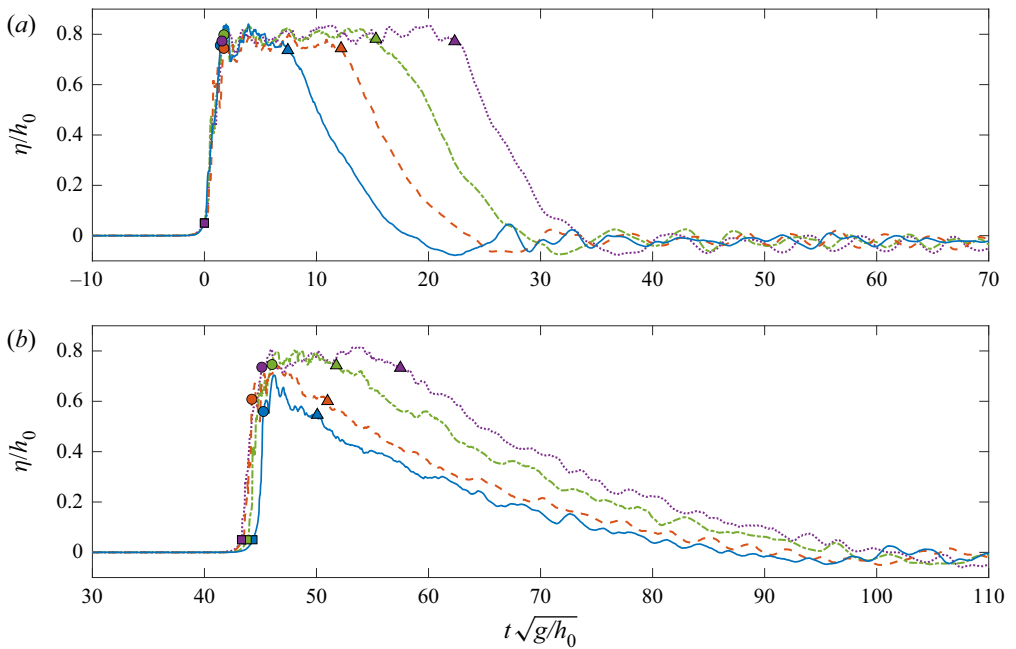


Figure 4. Time histories of dimensionless free surface elevations for BBs with  $F_{in} = 1.6$  at: (a) at CG1 and (b) at CG4. For the remainder of the caption see figure 2.

Surf and swash flows generated by bores

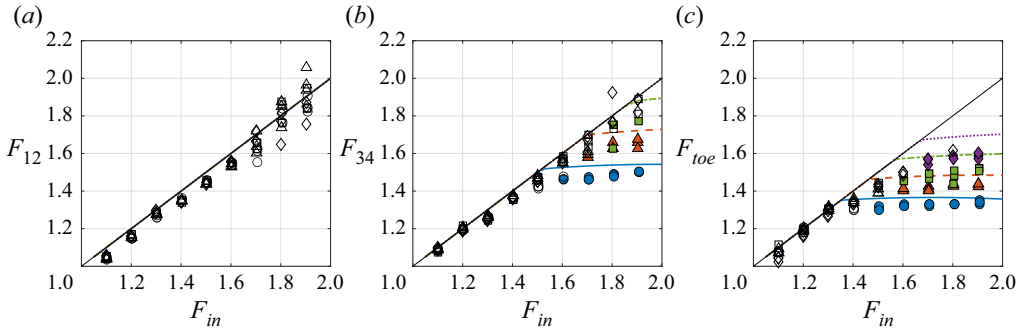


Figure 5. Comparisons between the input bore strength,  $F_{in}$  and the measured bore strengths: (a)  $F_{12}$ , (b)  $F_{23}$  and (c)  $F_{10e}$ , for different stroke lengths and bore strengths. Results for  $L_p/h_0 = 13.33$  are plotted in circles;  $L_p/h_0 = 20$  in triangles;  $L_p/h_0 = 26.67$  in squares; and  $L_p/h_0 = 33.33$  in diamonds. The unfilled markers represent non-decaying bores and the filled markers decaying bores. The solid black line represents the input bore strength and coloured lines represent the calculated bore strength for decaying bores using the method of characteristics (Lax 1948, Appendix B).

decreases and the bore tail becomes milder and longer as bores travel from CG1 to CG4. As shown in figure 4 for the BBs,  $F_{in} = 1.6$ , the shorter bore arrives at CG4 later than the longer bores do. For the shorter bores with  $L_p/h_0 = 13.33$  and 20, the bore plateau has disappeared at CG4 (i.e. the tail has reached the bore front). Also, the bores generated with the same stroke length become shorter for larger bore strengths.

The bore strength between two adjacent wave gauges (e.g. from CGi to CGj) can be approximately estimated by using the bore front arrival times at the gauges and the distance between the gauges as

$$F_{ij} = \frac{x_i - x_j}{(t_i - t_j)\sqrt{gh_0}}, \tag{3.6}$$

where  $x_i$  and  $x_j$  are the locations of the gauges (see table 1), and  $t_i$  and  $t_j$  denote the bore arrival times at the respective gauges. The strength of the bore travelling from CG5 to CG6 is designated as  $F_{10e}$  herein. The measured bore strengths  $F_{12}$ ,  $F_{34}$  and  $F_{10e}$  are plotted in figure 5 for different input bore strengths,  $F_{in}$ , at the wavemaker. All the data collected in configuration 1 of the laboratory experiments are included in the figure.

For non-decaying bores, the bore strength remains a constant in the constant depth region, as expected (see figure 5a). Bores with bore strength larger than 1.6 show noticeable data scatter, which is within  $\pm 5\%$  of the averaged values of the three repeated experiments with the same experimental condition. These bores possess a steep aerated front (see figure 4), resulting in larger scatter in the data for estimating the bore front arrival time, which, in turn, affects the estimations of bore front propagation speed and bore strength. The detailed explanations of the data scatter are provided in the supplementary material.

For bores generated by a shorter stroke with sufficient bore strength at the wavemaker, the bore lengths become progressively smaller as the bore front propagates towards the beach. Eventually, the bore tail catches up with the bore front and the bore height and bore strength starts to decrease, as indicated in figures 5(b) and 5(c). These features belong to a decaying bore. In this paper, the decaying bore is specifically defined as  $F_{34}$  and  $F_{10e}$  being less than 95% of  $F_{12}$ . For decaying bores, the evolution of their strengths in the constant depth region can be theoretically estimated by using the method of characteristics (Lax 1948). For completeness, the method of characteristics is briefly

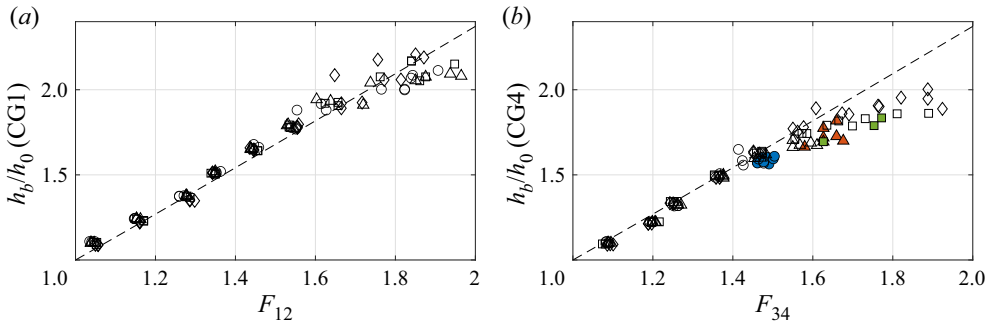


Figure 6. Measured bore heights for different stroke lengths and measured bore strengths: (a) CG1 and (b) CG4. Results for  $L_p/h_0 = 13.33$  are plotted in circles;  $L_p/h_0 = 20$  in triangles;  $L_p/h_0 = 26.67$  in squares; and  $L_p/h_0 = 33.33$  in diamonds. Unfilled markers represent non-decaying bores and filled markers decaying bores. Dashed line represents the theoretical bore height corresponding to a given bore strength (3.3).

described in Appendix B. The bore strength results based on the method of characteristics, which are slightly higher than the measurements, are also plotted in figures 5(b) and 5(c). The relative mean differences between the measured and the predicted bore strengths, using the bore relations for non-decaying bores and the method of characteristics results for decaying bores, are less than 3% for  $F_{12}$  and  $F_{34}$ , and 4% for  $F_{10e}$ , respectively. The measured bore strength is consistently smaller than the predicted one. The fact that these differences are maintained along the flume suggests that the discrepancy could be caused by the imperfection in the bore generation mechanism (i.e. the wavemaker generates a slightly weaker bore than expected) and the discrepancy remains in the measurements throughout the entire wave flume. The coefficient of determination  $R^2$  value between all the bore strength measurements  $F_{12}$ ,  $F_{34}$  and  $F_{10e}$  and the predicted bore strengths is  $R^2 = 0.919$ .

The bore height measurements at CG1 and CG4 are plotted against the measured bore strength  $F_{12}$  and  $F_{34}$  in figure 6. While the measured bore heights agree well with the theoretical predictions for both decaying and non-decaying bores, based on the bore relation, (3.3), the measured bore heights are lower than the predicted at CG4 for  $F_{34} > 1.6$ , which corresponds to very short and decaying bores.

The measured effective bore periods at CG1 and CG4 for the non-decaying bores are plotted against  $F_{in}$  in figure 7, showing good agreement with (3.4). The bore length and duration for decaying bores do not exist. Thus, no comparison is made in figure 7.

#### 4. Inundation depth and runup height

The time histories of the free surface elevations measured at the still water shoreline for UBs ( $F_{in} = 1.1$ ), UBBs ( $F_{in} = 1.4$ ) and BBs ( $F_{in} = 1.6$ ) are plotted in figures 8, 9 and 10, respectively. For the purpose of comparison, the measurements have been synchronized at the bore arrival time at the still water shoreline. Because of the steep free surface slope in UBs, signal dropouts can be seen in the ultrasound sensor records.

As shown in figure 8, the free surface shapes of the leading three undulations of the UBs are practically the same for different stroke lengths, resulting in a similar maximum inundation depth,  $I/h_0$ , denoted by circles. Moreover, an undulating plateau is formed for each case with a longer plateau for a longer stroke length. For the UBBs and BBs, a longer  $L_p/h_0$  produces a deeper inundation depth. However, there is no evidence that the maximum inundation depth has been reached (i.e. a longer bore with same  $F_{in}$  may

Surf and swash flows generated by bores

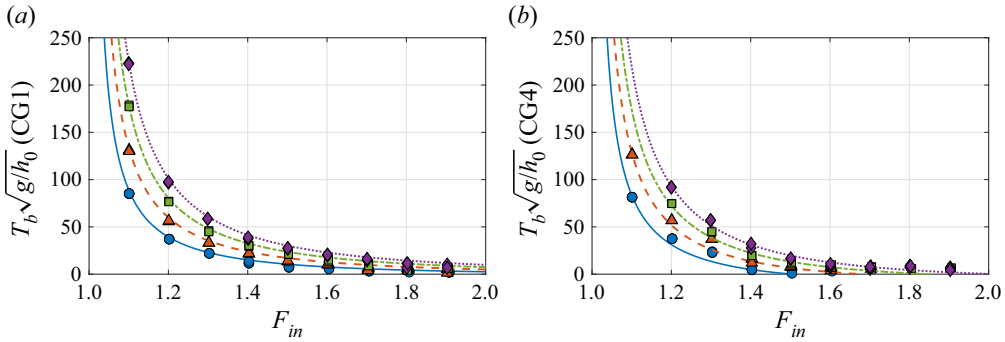


Figure 7. Effective bore periods measured for different stroke lengths and bore strengths at: (a) CG1 and (b) CG4. Results for  $L_p/h_0 = 13.33$  are plotted in circles;  $L_p/h_0 = 20$  in triangles;  $L_p/h_0 = 26.67$  in squares; and  $L_p/h_0 = 33.33$  in diamonds. Coloured lines are calculated using (3.4), where  $x_t$  is the location of the respective capacitance gauge (see table 1) and  $F_{in}$ ,  $h_0$  and  $L_p$  correspond to the input parameters.

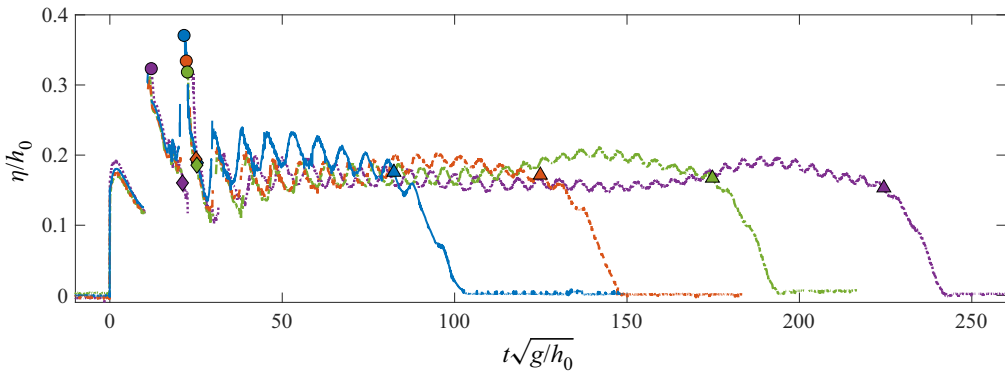


Figure 8. Time histories of dimensionless free surface elevations at the still water shoreline for UBs with  $F_{in} = 1.1$ . Blue line:  $L_p/h_0 = 13.33$ ; dashed orange line:  $L_p/h_0 = 20$ ; dashed-dotted green line:  $L_p/h_0 = 26.67$ ; dotted purple line:  $L_p/h_0 = 33.33$ . Circles: maximum free surface height ( $I/h_0$ ); diamonds: the beginning of the flood plateau; triangles the end of flood plateau.

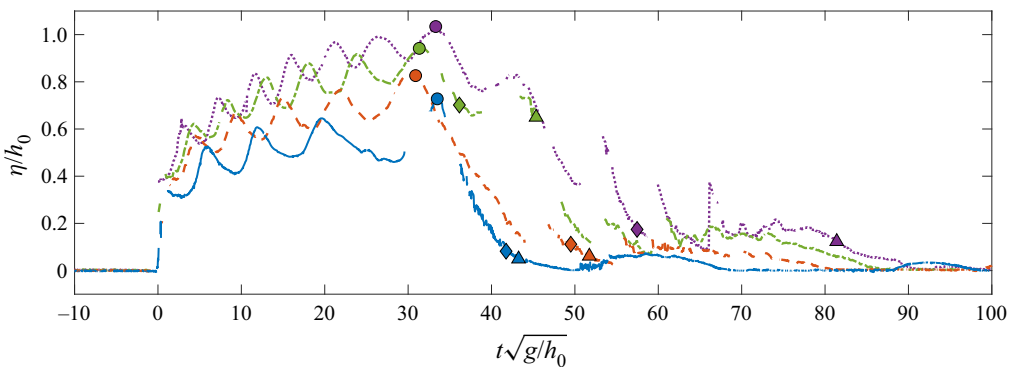


Figure 9. Time histories of dimensionless free surface elevations at the still water shoreline for UBs with  $F_{in} = 1.4$ . For the rest of caption see figure 8.

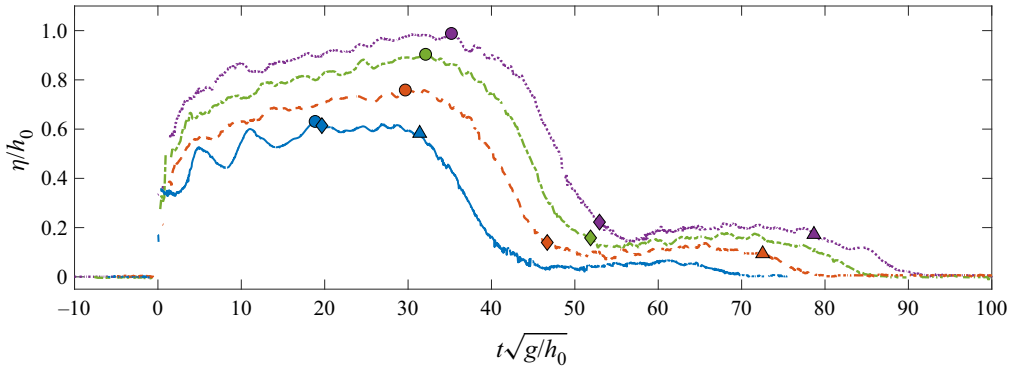


Figure 10. Time histories of dimensionless free surface elevations at the still water shoreline for BBs with  $F_{in} = 1.6$ . For the rest of caption see figure 8.

generate a even higher inundation depth). In addition, none of the cases shows the presence of a flood plateau (i.e. no quiescent water was observed following the bore runup). Based on the laboratory bore strength measurements (figure 5), all the bores with  $F_{in} = 1.4$  are classified as non-decaying when reaching the beach toe. However, the bore length relation (3.5) predicts that bores generated with  $F_{in} = 1.4$  and  $L_p/h_0 = 13.33$  reach the beach toe as decaying bores ( $L_b/h_0 = -7.2$ ). The length of the bores reaching the beach toe for  $L_p/h_0 = 33.33$  is  $L_b/h_0 = 38.48$ . The minimum bore length necessary to reach the maximum inundation depth for  $F_{toe} = 1.4$  and  $s = 0.1$ , based on Barranco & Liu (2021) findings, is  $L_i/h_0 = 70.35$ , which is almost double the longest bore reaching the beach toe. For  $F_{in} = 1.6$  all the bores reaching the beach toe are classified as decaying. The strength of the bores reaching the beach toe,  $F_{toe}$ , for  $F_{in} = 1.6$  varies from 1.35 to 1.55 (see figure 5).

The beginning and the end of the flood plateau at the still water shoreline are identified with the methodology presented in Barranco & Liu (2021). The maximum inundation depths measured at the still water shoreline,  $I$ , are plotted vs  $F_{toe}$  in figure 11. The laboratory measurements are compared with the predictive formulas developed by Barranco & Liu (2021) (i.e. (5.1) and (5.2)). For each stroke length,  $L_p$ , (3.5) is used to calculate the corresponding  $L_b$  for a range of  $1.01 \leq F_{in} \leq 2$  with  $L_f = 23.7$  m. For non-decaying bores ( $L_b > 0$ ),  $F_{toe} = F_{in}$  as shown in figure 5. For decaying bores,  $L_b = 0$  is substituted in the predictive relation for short bores (Barranco & Liu 2021, (5.1)). The empirical relations generally under-predict the maximum inundation depths for  $F_{toe} < 1.4$ . The estimated maximum inundation depths for decaying bores fit well with the laboratory experiments and represent the lower limit of maximum inundation depths.

Similarly, the runup height measurements,  $R$ , are compared with solutions recommended by Miller (1968) and Barranco & Liu (2021) in figure 12. Good agreement for both non-decaying and decaying bores is observed. The bore strength at the slope toe shows data scatter for the weakest bores ( $F_{toe} \leq 1.2$ ). However, these cases produce almost identical runup. Miller (1968) and Barranco & Liu (2021) predict similar runup heights for the range of bore strengths analysed in this study. However, UBs and BBs have different slopes in Miller's work; a steeper slope for UBs and a milder one for BBs. The Miller (1968) formulas are given in terms of the bore height, and thus, to calculate the runup as a function of  $F_{toe}$ , (3.3) has been employed. It should be noted that Miller's formulas do not cover the range for  $1.25 < F_{toe} < 1.55$ .

In figure 13, the flood duration measurements,  $T_f$ , are plotted vs  $F_{toe}$  for bores with long enough bore length at the toe of the slope to generate a flood plateau (Barranco

Surf and swash flows generated by bores

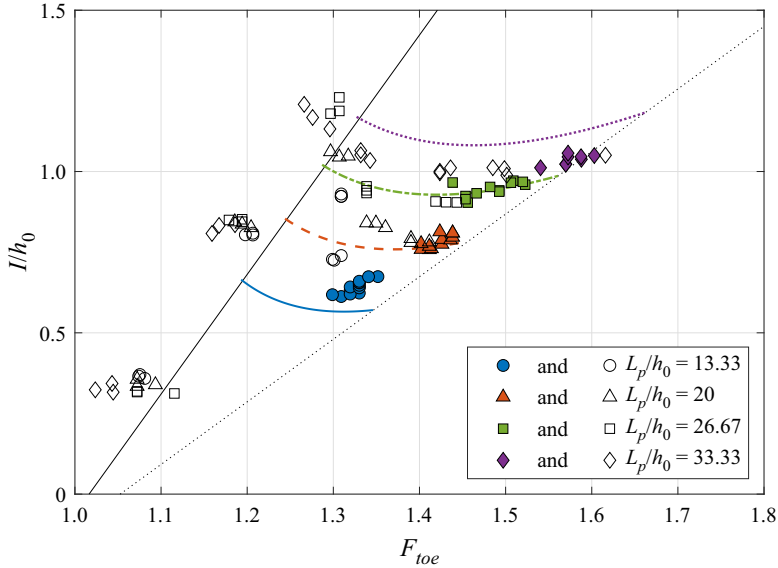


Figure 11. Dimensionless inundation depths at the still water shoreline,  $I/h_0$ , are plotted against the bore strength measured at the beach toe,  $F_{toe}$ , and the stroke length,  $L_p/h_0$ . Unfilled markers represent non-decaying bores and filled markers are for decaying bores. The black solid line represents the predictive relation for inundation depth produced by long bores (Barranco & Liu 2021). The dashed coloured lines are the predictive relations for short bores with different stroke length, in which  $L_b$  is calculated from (3.5) for each  $L_p$ , and the black dotted line shows the particular case for the predictive relation for short bores in which  $L_b = 0$  (i.e. decaying bores).

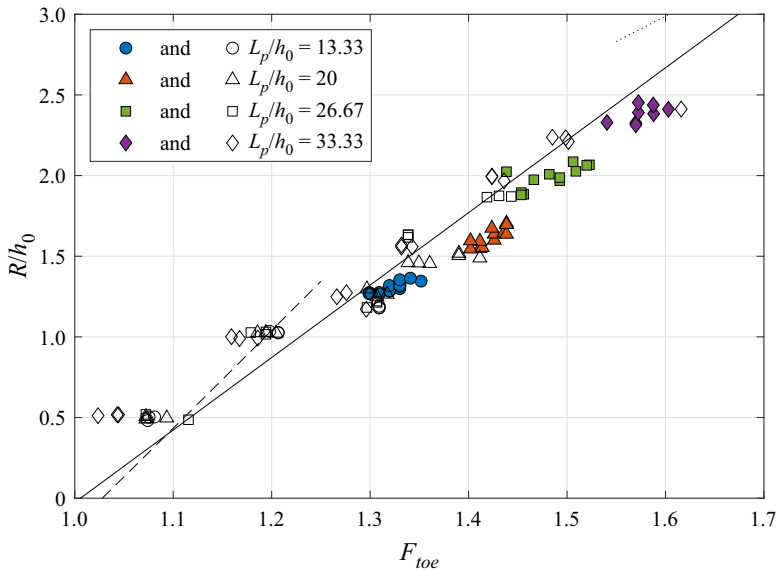


Figure 12. Dimensionless maximum runup,  $R/h_0$ , in terms of the bore strength at the beach toe,  $F_{toe}$  and the stroke length,  $L_p/h_0$ . Unfilled markers represent non-decaying bores and filled markers denote decaying bores. Dashed and dotted lines are solutions of the Miller (1968) predictive relations for UBs and BBs, respectively, and the solid line shows the Barranco & Liu (2021) predictive relation for runup heights.

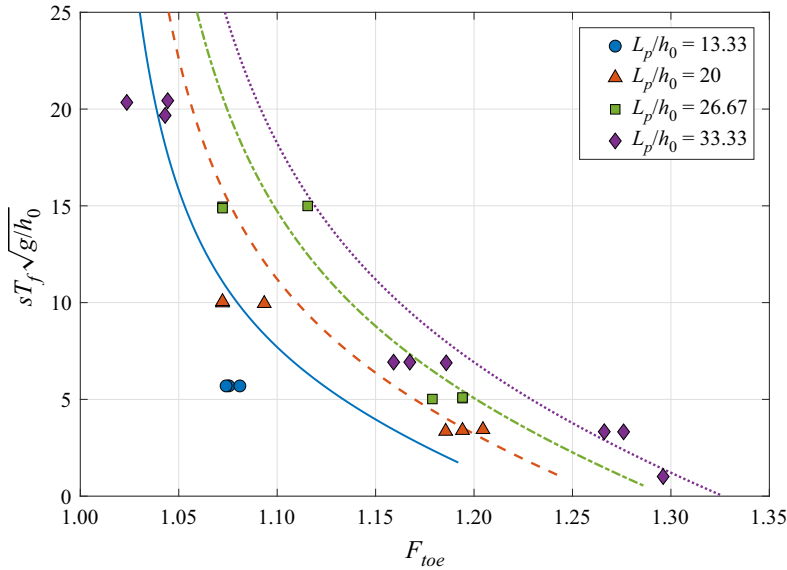


Figure 13. Dimensionless flood duration at the still water shoreline,  $sT_f \sqrt{g/h_0}$ , in terms of the bore strength at the beach toe,  $F_{toe}$  and the stroke length,  $L_p/h_0$ . Solid coloured lines represent the solutions from Barranco & Liu (2021), in which  $L_b$  is calculated using (3.5).

& Liu 2021). Only the weakest bores are observed to produce a flood plateau, which lasts longer for longer stroke lengths. The predictive relation is close to the laboratory measurements for  $F_{toe} > 1.15$ , while the flood durations for weaker bores are generally overestimated. Similar differences for weak bores were observed in Barranco & Liu (2021).

The  $R^2$  values between the laboratory observations and the formulas developed by Barranco & Liu (2021) are as follows:  $R^2 = 0.544$  for the maximum inundation depth,  $R^2 = 0.878$  for the maximum runup height and  $R^2 = 0.978$  for the flood duration. While the predicted maximum inundation depths are fairly close to those measured, as shown in figure 11, the relatively low  $R^2$  value is not entirely surprising. From figures 8 and 9 it is shown that, in the case of UBs, the maximum inundation depth depends not only on the bore height but also on the height of the leading undulations. From figure 2 it is also clear that the leading undulations evolve as the bore propagates, increasing in amplitude, which is a well-known process (El 2007; Grimshaw, Zhang & Chow 2007; Brühl *et al.* 2022). Therefore, differences in the propagation distance between the bore generation mechanism and the slope will affect the maximum inundation depth measurements. Moreover, differences in the bore generation mechanism itself will affect the initial shape of the leading undulations, potentially affecting the leading undulations evolution, and thus, the maximum inundation depth. It is also observed from figures 8 and 9 that undulations in the flood plateau may affect the flood duration measurements, especially for short bores in which relatively large undulations are present during the entire flood duration.

On the other hand, short and decaying bores produce runup values generally lower than those produced by longer bores and that predicted by Barranco & Liu (2021) (see figure 12). While the bore length and slope are not identified as predictor variables for the bore runup in Barranco & Liu (2021), the study does not include decaying bores. Bores which decay in constant depths will continue to decay as they climb up on a slope, reaching the still shoreline with a bore front velocity lower than the strength that a non-decaying

bore would achieve. Thus, it is predicted that the bore length at the beach toe and the slope may have a small influence on the maximum runup height for very short and decaying bores. The hypothesis is supported by the results in [figure 12](#).

## 5. The HSPIV velocity measurements in constant depth

Using HSPIV images, the free surface location can first be identified. For BBs the images show air bubbles, and the free surface is defined as the lower boundary of the aerated flow region. The details for identifying the free surface location from HSPIV images are provided in [Appendix C](#). For each experimental condition, 10 repetitions are conducted. The velocity measurements are decomposed into the ensemble-averaged velocity,  $(\bar{u}, \bar{w})$ , and the fluctuating velocity  $(u', w')$ , i.e.  $u_i(x, z, t) = \bar{u}(x, z, t) + u'_i(x, z, t)$  and  $w_i(x, z, t) = \bar{w}(x, z, t) + w'_i(x, z, t)$ , where the subscript 'i' corresponds to the 'ith' repetition. The magnitude of the fluctuating velocity is represented by the root mean squared (r.m.s.) value of the 10 repetitions. The time origin ( $t = 0$ ) of the experiments is set at the arrival of the bores at the beach toe ( $x = 0$ ).

Generally speaking, it is desirable to perform a large number of repetitive experiments so as to obtain meaningful turbulence statistics (O'Donoghue *et al.* 2010). It is shown in the supplementary material that the converged ensemble-averaged and fluctuating velocities can be achieved at FOV1 for the BB cases, if more than 7 repetitions are conducted. The flows in the BB case and in the swash flow of the undulating bore case show wave breaking, suggesting that the observed fluctuating velocities could be related to turbulence. However, for the following reasons the measured fluctuating velocities will not further be characterized as turbulence: (i) in the present experiments, the spanwise velocity components are not measured. Therefore, the collected data are not sufficient for defining the three-dimensional vorticity field, which is the essential ingredient for properly describing turbulence. (ii) The resolutions in the velocity measurements are limited so that the turbulence dissipation cannot be directly calculated and the full extent of the inertial sub-range in the spatial spectra of the fluctuating velocities cannot be clearly revealed (the spatial spectrum plots are provided in the supplementary material). Nevertheless, the information on the fluctuating velocities will be reported herein as a reference.

### 5.1. Undulating bore

The time histories of the dimensionless ensemble-averaged horizontal and vertical velocities for the UB ( $F_{in} = 1.1$ ) at FOV1 ( $x = -9.87$  m) are plotted in [figure 14](#). The resolution for the UB HSPIV measurements at FOV1 is 2.3 mm and the FOV dimension is  $0.144 \times 0.294$  m. The maximum flow velocity measurable with this FOV resolution is  $0.575 \text{ m s}^{-1}$ . The time history of the free surface undulations is also shown. The horizontal velocities fluctuate between the crests and troughs of the free surface, converging to the mean free surface elevation at  $z/h_0 = 1.11$  in an oscillatory manner. The records are truncated so that the reflection from the beach is not shown. The vertical velocities also exhibit oscillatory behaviour and their magnitudes decrease in time as free surface undulations diminish. Overall, the vertical velocities are weaker than the horizontal velocities. The horizontal velocity appears to be quite uniform in the water column. Since the UB does not break, fluctuating velocities are negligibly small in the HSPIV measurements and are not investigated here.

The vertical profiles of the horizontal and vertical velocities in the water column at several phases during the first three undulations are plotted in [figure 15](#). These selected phases comprise the crests and troughs of the undulations (unfilled markers) and the

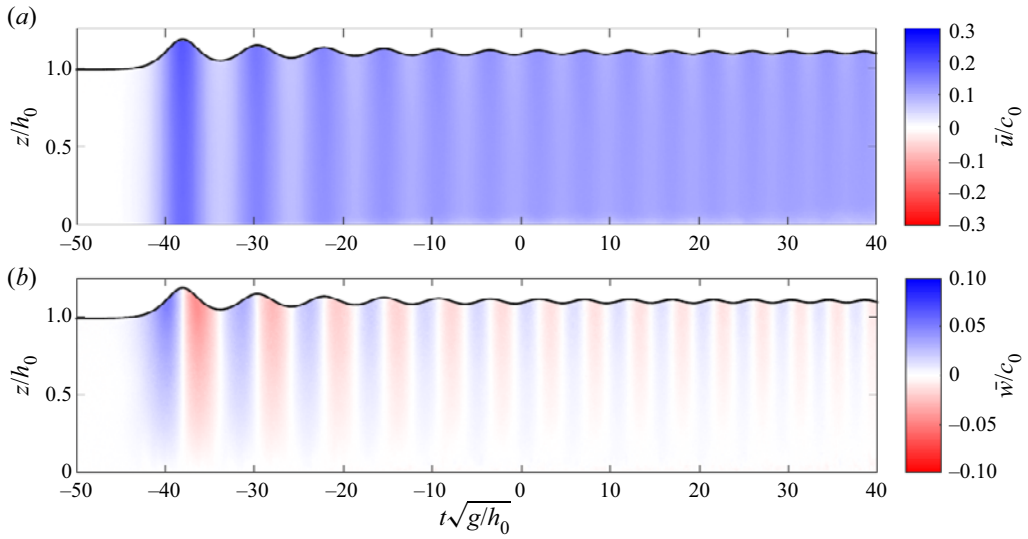


Figure 14. Time histories of free surface elevation and dimensionless ensemble-averaged mean velocities in the water column at  $x = -9.87$  m for  $F_{in} = 1.1$ . (a) The horizontal velocity component, and (b) the vertical velocity component.

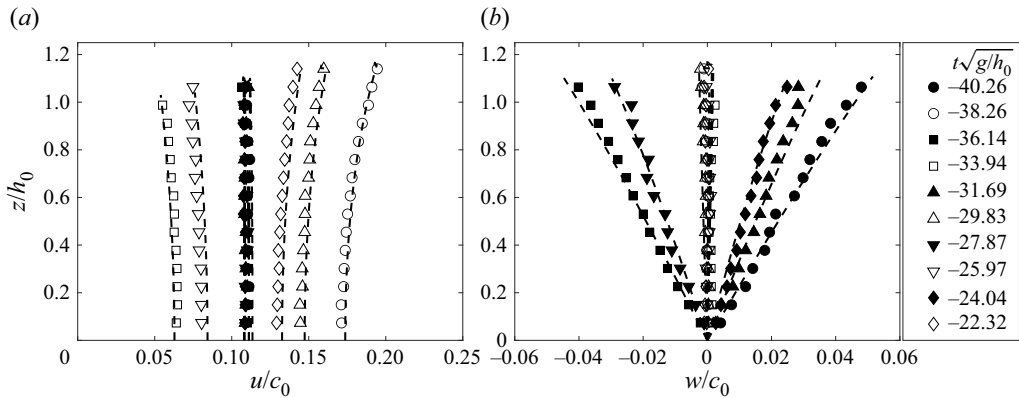


Figure 15. Vertical profiles of velocity components in water column for  $F_{in} = 1.1$  at  $x = -9.87$  m. (a) The dimensionless horizontal velocities, and (b) the dimensionless vertical velocities. Dashed lines represent the velocity components under the train of solitary waves (see figure 16).

times when the free surface elevation intersects with the mean elevation  $z/h_0 = 1.11$  (filled markers). The horizontal velocities are very close to uniform in the water column for all phases. However, the velocities at the free surface tend to be larger, especially under the crests. The magnitudes of the horizontal velocities converge to  $u/c_0 = 0.11$  in an oscillatory manner. The vertical velocities vary almost linearly in the water column, being zero at the bottom and reaching a maximum at the free surface, which is a typical long-wave characteristic. Under the crests and troughs of undulation the vertical velocities are close to zero in the entire water column. The magnitudes of the vertical velocities converge to zero as the free surface undulations subside. The vertical profiles of the ensemble-averaged velocity components in the water column are similar to those reported in Lin *et al.* (2020b), in which the UB was generated by a dam-break system.

### Surf and swash flows generated by bores

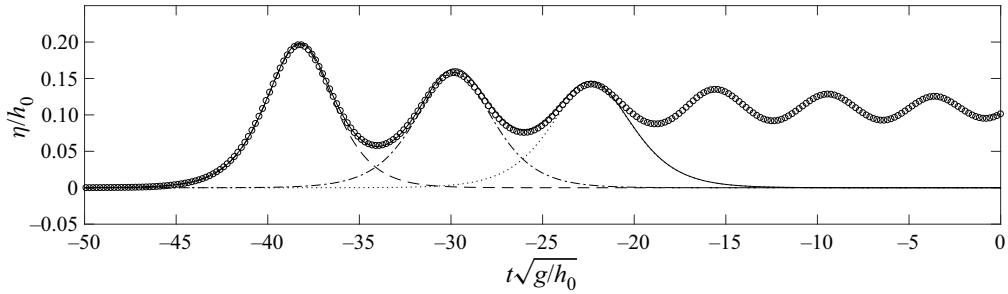


Figure 16. Time histories of ensemble-averaged free surface elevations at  $x = -9.87$  m for  $F_{in} = 1.1$  (circles). Free surface elevations of three solitary waves with  $H/h_0 = 0.20$  (dashed line),  $0.16$  (dashed-dotted line) and  $0.14$  (dotted line). The superposition of these three solitary waves is shown by the solid line.

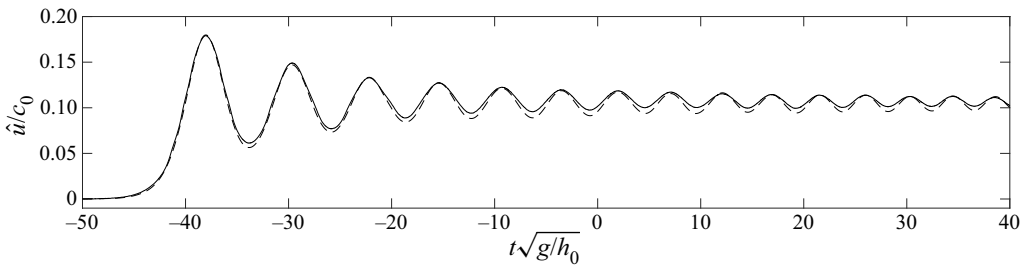


Figure 17. Time histories of dimensionless depth-averaged velocity at  $x = -9.87$  m. The solid line denotes the HSPIV data for  $F_{in} = 1.1$  and the dashed line represents the theoretical estimation using (5.1).

It is well known (El 2007; Grimshaw *et al.* 2007; Brühl *et al.* 2022) that undulating bores will eventually evolve into a train of solitary waves with the amplitude of the leading solitary wave being twice that of the bore plateau. In the present experiments the amplitude of the leading undulation at FOV1 is estimated as  $\eta/h_0 = 0.19$ , which is slightly less than twice that of the bore plateau ( $\eta/h_0 = 0.11$ ). To gain more insights, in figure 16 three solitary wave free surface profiles with different wave heights are superimposed with those of the measured leading surface undulations. Specifically, the solitary wave crests are matched with those of the corresponding undulating crests, and the solitary wave profiles are obtained by employing the Grimshaw (1970) third-order solutions with  $H/h_0 = 0.20$ ,  $0.16$  and  $0.14$ , respectively, in a water depth of  $h_0 = 0.24$  m. A train of solitary waves is then calculated by superimposing linearly the three waves. The corresponding horizontal and vertical flow velocities for the train of solitary waves have also been plotted in figure 15. The free surface elevation and flow velocities of the leading undulation of the UB agree with those of the solitary wave train very well. The second and third undulations are less developed with respect to the solitary forms, requiring more travel time and distance to evolve into individual solitary waves with different wave heights.

The time history of the measured ensemble- and depth-averaged horizontal velocity at  $x = -9.87$  m is plotted in figure 17. Based on the long-wave theory, the depth-averaged velocity can be estimated as

$$\hat{u} = \frac{\eta\sqrt{g(h_0 + \eta)}}{h_0 + \eta}, \quad (5.1)$$

which is also plotted in figure 17, showing an excellent agreement.

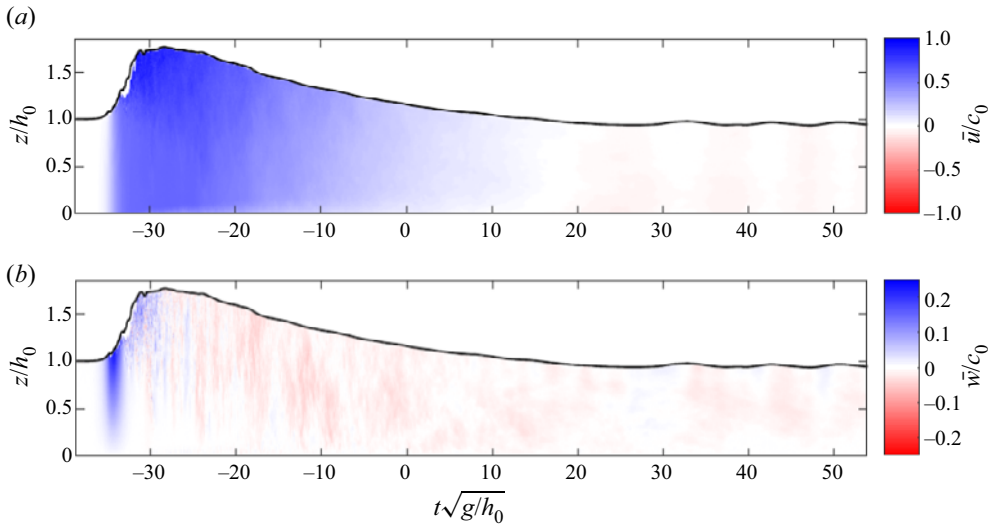


Figure 18. Time histories of free surface elevation and the ensemble-averaged velocities in the water column at  $x = -9.87$  m for BB. Here,  $F_{in} = 1.6$ . (a) Horizontal velocity component and (b) vertical velocity component.

### 5.2. Breaking bore

For BBs the bore front is always aerated and a significant number of air bubbles are entrained into the water body behind the bore front. Some of the HSPIV images of breaking bores are shown in [Appendix C](#), and the identification of the aerated free surface is also discussed in the same appendix.

The time histories of the dimensionless ensemble-averaged velocity components at FOV1 ( $x = -9.87$  m) for the BB ( $F_{in} = 1.6$ ) are plotted in [figure 18](#). The resolution for the BB HSPIV measurements at FOV1 is 2.6 mm and the FOV dimension is  $0.143 \times 0.380$  m. The maximum flow velocity measurable with this resolution is  $0.65 \text{ m s}^{-1}$ . Overall, both horizontal velocity and vertical velocity components increase drastically at the arrival time of the BB. They are of the same order of magnitude at the bore front. However, the horizontal velocity becomes more dominant as the bore passes through.

Velocity profiles in the water column at different time instants are also shown in [figure 19](#). As shown in [figure 19\(a\)](#), during the bore front period ( $-35 < t\sqrt{g/h_0} < -32$ ) the horizontal velocity accelerates quickly, especially near the free surface. During this period the horizontal velocity profiles remain more or less uniform below the still water surface,  $z/h_0 = 1$ , and above the still water level the horizontal velocity profiles become linear, generating strong vorticity. Meanwhile, the vertical velocities ([figure 19b](#)) have a linear profile. The considerable data scatter above the still water level is associated with the turbulence and bubbles on the breaking front. At the bore arrival time ( $t\sqrt{g/h_0} \simeq -34.30$ , shown by  $\circ$ ) the vertical velocity is of the same order of magnitude as the horizontal velocity near the free surface. However, the vertical velocity decelerates quickly in time while the horizontal velocities accelerate, dominating the flow at the peak of the bore front ( $t\sqrt{g/h_0} \simeq -32.34$ , shown by  $\square$ ). During the bore plateau ( $-32 < t\sqrt{g/h_0} < -26$  in [figure 19c,d](#)) a uni-directional flow field is formed in which the vertical velocity fluctuates around zero, being one order of magnitude smaller than the horizontal velocity. Moreover, the horizontal velocity is uniform in the direction of bore propagation, except near the free surface. The strength of the vorticity above the still water level appears to decrease slightly

Surf and swash flows generated by bores

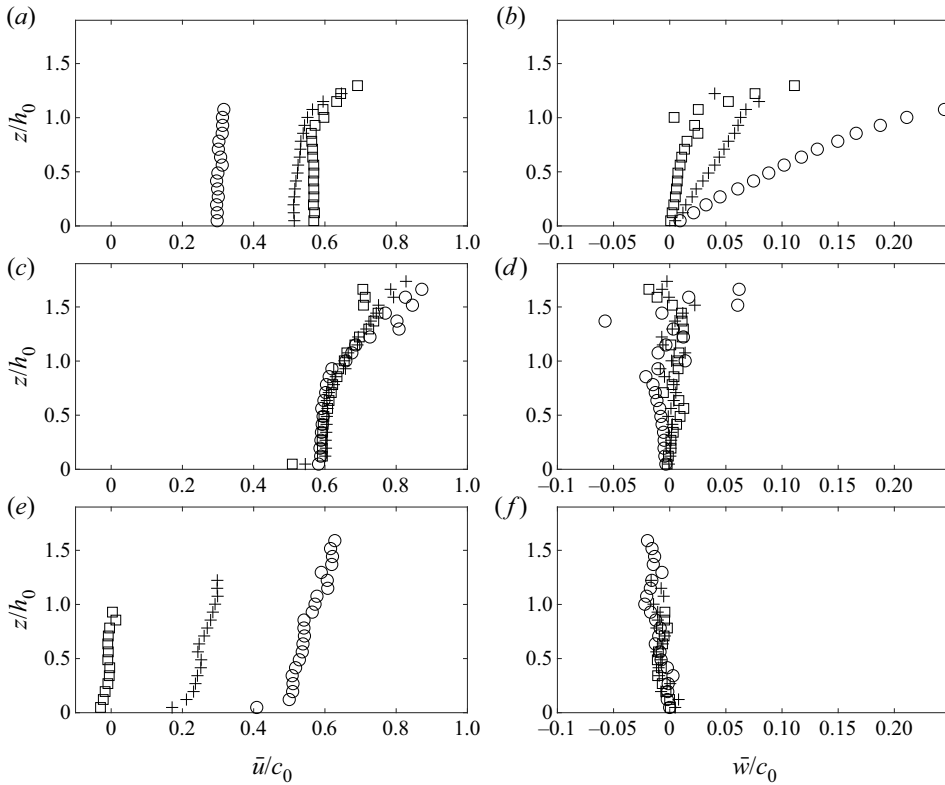


Figure 19. Vertical profiles of ensemble-averaged velocities in the water column at  $x = -9.87$  m for bore with  $F_{in} = 1.6$ . (a,c,e) Show the magnitudes of horizontal velocity component and (b,d,f) display the magnitudes of vertical velocity component. Panels (a,b)  $\circ$ :  $t\sqrt{g/h_0} = -34.30$ ;  $+$ :  $t\sqrt{g/h_0} = -33.23$ ;  $\square$ :  $t\sqrt{g/h_0} = -32.34$ . Panels (c,d)  $\circ$ :  $t\sqrt{g/h_0} = -30.56$ ;  $+$ :  $t\sqrt{g/h_0} = -27.96$ ;  $\square$ :  $t\sqrt{g/h_0} = -25.37$ . Panels (e,f)  $\circ$ :  $t\sqrt{g/h_0} = -20.92$ ;  $+$ :  $t\sqrt{g/h_0} = -6.09$ ;  $\square$ :  $t\sqrt{g/h_0} = 19.12$ .

and diffuse downwards into the water column. The thin bottom boundary layer structure can also be seen in this figure. Finally, figures 19(e) and 19(f) show that, during the bore tail ( $-26 < t\sqrt{g/h_0} < 15$ ), both horizontal and vertical velocities decrease rapidly and the flow remains practically uni-directional. The vorticity generated near the BB front has diffused further downwards into the water column below the still water level and has merged with the bottom boundary layer.

The time history of the depth- and ensemble-averaged horizontal velocities at  $x = -9.87$  m for the BB is plotted in figure 20. The depth-averaged horizontal velocities are calculated employing the bore relations (3.1), (3.2) and (3.3) with the relationship  $\beta = 2c - u$ . During the bore front period ( $t\sqrt{g/h_0} < -31.53$ ) the bore strength and bore flow velocities are calculated from the free surface measurements and bore relations. During the bore plateau and bore tail periods, the depth-averaged velocities are calculated employing  $\beta = 2c_b - u_b$ , which is a constant (see Appendix A). During the bore front period, the measured depth-averaged flow velocities are larger than the calculated values employing the HSPIV data and lower than the calculated values using the capacitance gauges data. During the bore plateau and bore tail periods, the measured depth-averaged flow velocities are similar to those calculated employing both the HSPIV data and the

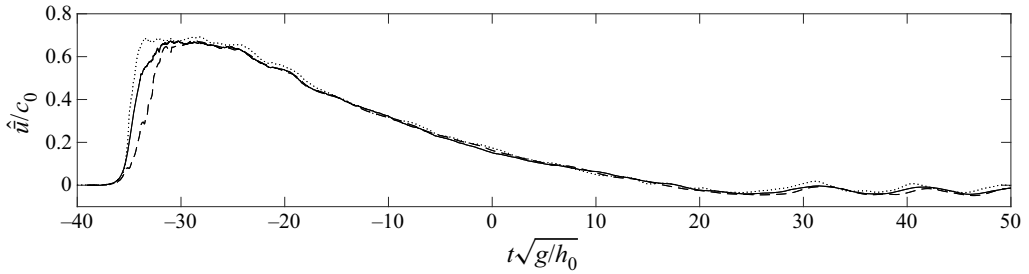


Figure 20. Time histories of the depth- and ensemble-averaged horizontal velocity at  $x = -9.87$  m. Here,  $F_{in} = 1.6$ . Solid line: HSPIV velocity data; dashed line: calculated from the bore relations employing the HSPIV free surface measurements; dotted line: calculated from the bore relations employing the CG free surface measurements.

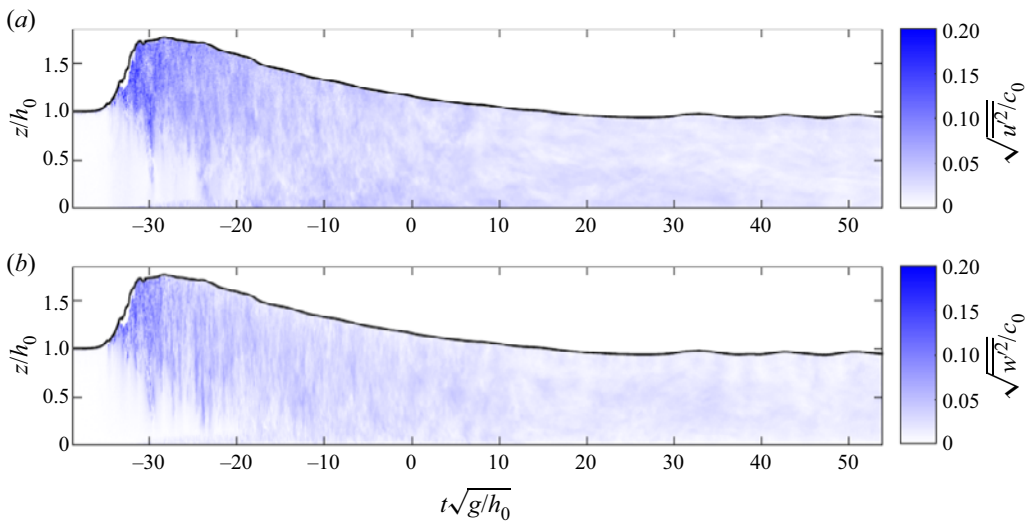


Figure 21. Time histories of free surface elevation and r.m.s. values of fluctuating velocities in the water column at  $x = -9.87$  m for bore with  $F_{in} = 1.6$ . (a) The magnitude of horizontal fluctuating velocity component and (b) the magnitude of vertical fluctuating velocity component.

capacitance gauges data. It is also important to notice that the bore flow velocities near the free surface are significantly larger than the depth-averaged velocities.

The time histories of the dimensionless ensemble-averaged fluctuating velocities at FOV1 ( $x = -9.87$  m) for the BB ( $F_{in} = 1.6$ ) are plotted in figure 21. Overall, as compared with the ensemble-averaged velocity components, figure 18, the magnitude of the fluctuating velocity is almost one order smaller. The largest fluctuating velocities are observed in the vicinity of the bore front. After the bore front, fluctuating velocities gradually cover the entire water column.

Several profiles of the fluctuating velocity in the water column at different time instants are also shown in figure 22. As shown in figure 21, the largest fluctuating velocities are observed near the BB front. Smaller fluctuating velocities are later observed in the entire water column at the bore plateau and bore tail. Before the arrival of the bore front (i.e.  $t\sqrt{g/h_0} < -37.00$ ) the fluctuating velocities are negligible and the largest normalized fluctuating velocities are smaller than  $10^{-3}$ . During the bore front period ( $-34.30 < t\sqrt{g/h_0} < -32.34$ ; figure 22a,b) the fluctuating velocities are concentrated above the

Surf and swash flows generated by bores

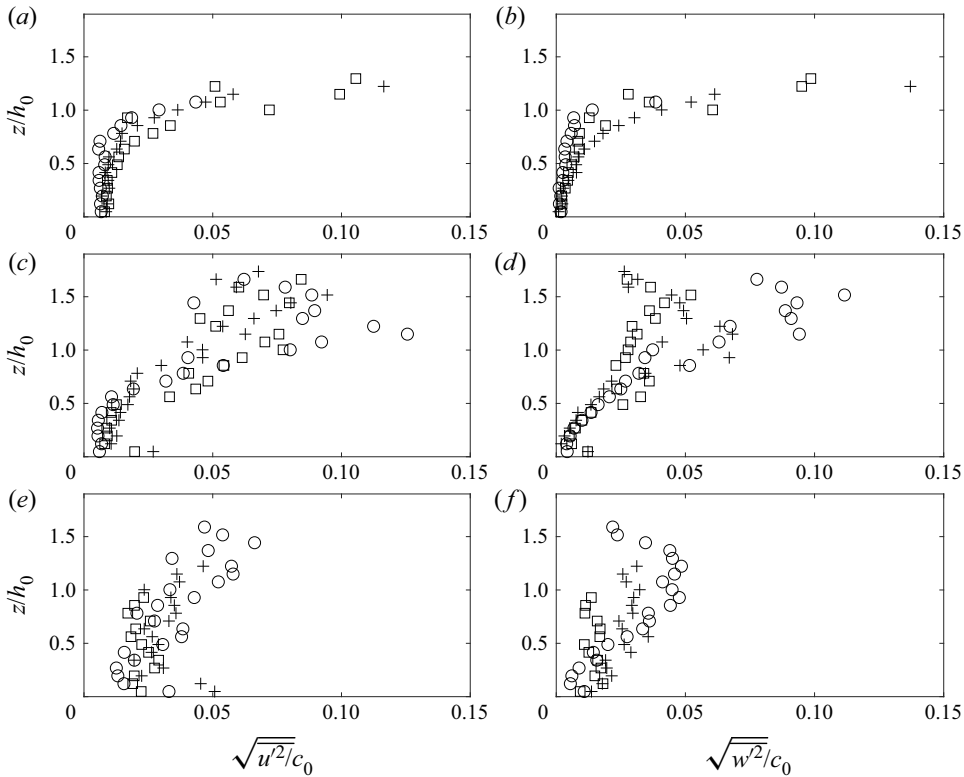


Figure 22. Vertical profiles of the r.m.s. value of the fluctuating velocity in the water column at  $x = -9.87$  m for bore with  $F_{in} = 1.6$ . (a,c,e) Display the magnitudes of the horizontal component and (b,d,f) show the magnitude of the vertical component. Panels (a,b)  $\circ$ :  $t\sqrt{g/h_0} = -34.30$ ;  $+$ :  $t\sqrt{g/h_0} = -33.23$ ;  $\square$ :  $t\sqrt{g/h_0} = -32.34$ . Panels (c,d)  $\circ$ :  $t\sqrt{g/h_0} = -30.56$ ;  $+$ :  $t\sqrt{g/h_0} = -27.96$ ;  $\square$ :  $t\sqrt{g/h_0} = -25.37$ . Panels (e,f)  $\circ$ :  $t\sqrt{g/h_0} = -20.92$ ;  $+$ :  $t\sqrt{g/h_0} = -6.09$ ;  $\square$ :  $t\sqrt{g/h_0} = 19.12$ .

still water level ( $z/h_0 > 1$ ), near the aerated flow, which has a strong correlation with breaking. Fluctuating velocities are also visible in  $0 < z/h_0 < 0.5$ . At  $t\sqrt{g/h_0} = -34.3$  and  $z/h_0 = 0.5$  the ensemble-averaged velocities are  $\bar{u} = 0.4$  m s<sup>-1</sup> and  $\bar{w} = 0.125$  m s<sup>-1</sup> (i.e. the vertical ensemble-averaged velocities near the toe of the bore front are of the same order of magnitude as the horizontal ensemble-averaged vertical velocities). Moreover, the vertical ensemble-averaged velocities accelerate and decelerate during the bore front arrival, creating a shear flow (i.e.  $\partial u/\partial z \neq 0$  and  $\partial w/\partial x \neq 0$ ). During the bore plateau period (figure 22c,d) the horizontal and vertical fluctuating velocity profiles vary in time above  $z/h_0 > 0.5$ , indicating that the magnitude of the fluctuating velocity decreases in time. In addition, more fluctuating velocities are observed deeper into the water column. The fluctuating velocities are also observed near the bottom boundary, which appear to be much weaker than their counterpart. These fluctuating velocities could be triggered by the uneven bottom in the junction between the flume steel bottom and the glass window installed to carry out PIV measurements. During the bore tail period (figure 22e,f), the fluctuating velocities are present in the entire water column. Overall, throughout the entire process, the horizontal fluctuating velocities are always of the same order of magnitude of the vertical fluctuating velocities.

The time history of the depth-averaged r.m.s. values of horizontal and vertical fluctuating velocities at  $x = -9.87$  m for the BB is plotted in figure 23. Both the horizontal

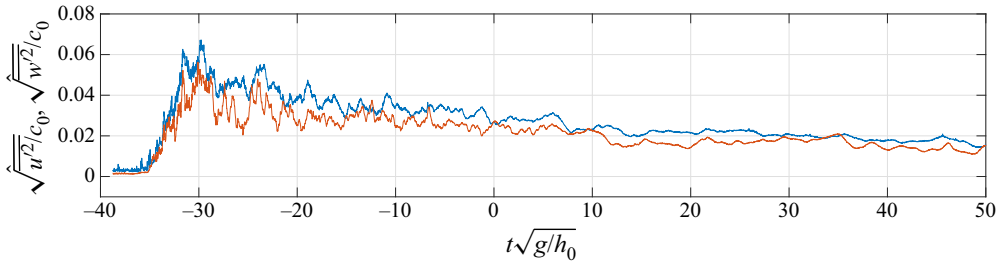


Figure 23. Time histories of the depth-averaged r.m.s. values of the fluctuating velocity at  $x = -9.87$  m. Here,  $F_{in} = 1.6$ . Blue line: the horizontal component; orange line: the vertical component.

and vertical fluctuating velocities first increase until reaching their maxima at the arrival of the bore front, and then they decrease steadily during the bore plateau and bore tail. Although the depth- and ensemble-averaged flow velocities are close to zero after the bore tail ( $t\sqrt{g/h_0} > 20$ , see figure 20), the presence of fluctuating velocities after the bore has passed is considerable, close to 1/3 of the fluctuating velocity magnitude at the bore front arrival. In general, the horizontal fluctuating velocity component is slightly larger than the vertical component, although both components meet at similar values at irregular intervals.

## 6. The HSPIV velocity measurements in the swash

### 6.1. Undulating bore

The time histories of the ensemble-averaged velocity components for the UB case at FOV2 ( $X = 2.26$  m) are first plotted in figure 24. The resolution for the UB HSPIV measurements at FOV2 is 2 mm and the FOV dimension is  $0.321 \times 0.117$  m. The maximum flow velocity measurable with this resolution is  $0.5 \text{ m s}^{-1}$ . The detailed velocity profiles in the water column at selected time instants are also shown in figure 25. In these figures, the local coordinates ( $X, Z$ ) and the corresponding velocity components ( $U, W$ ) are used, in which ( $X, U$ ) are in the direction along the beach face, and ( $Z, W$ ) are normal to it (see figure 1).

As shown in figure 24, the ensemble-averaged velocity components oscillate under the surface undulations. The horizontal velocity changes from the onshore direction (positive) under an undulating crest to the offshore direction (negative) under an undulating trough, with the exception that, under the third undulating crest the velocity becomes almost zero. The vertical velocity also changes its direction accordingly. Both horizontal and vertical velocities are of the same order of magnitude and are nearly uniform in the water column. However, during the bore tail period, the down-rush flow becomes almost uni-directional and uniform, moving in the offshore direction. More detailed velocity profiles are presented in figure 25.

Figures 25(a) and 25(b) show the horizontal and vertical velocity profiles during the first undulation,  $9.64 < t\sqrt{g/h_0} < 19.39$ . The maximum onshore (positive) horizontal velocities are measured at the leading front of the bore (i.e.  $t\sqrt{g/h_0} = 9.64$ ). The onshore flow velocities decrease as the water depth decreases and turn into the offshore direction with negative values (i.e.  $t\sqrt{g/h_0} = 17.49$ ). However, the horizontal velocities become positive again, flowing in the onshore direction, with the arrival of the second undulating crest (i.e.  $t\sqrt{g/h_0} = 19.39$ ). The corresponding vertical velocity components also change direction accordingly; namely, the vertical velocity is negative (downwards) when the horizontal velocity is in the onshore direction and *vice versa*. During this period, the horizontal velocities are almost uniform in the water column and the vertical velocities

Surf and swash flows generated by bores

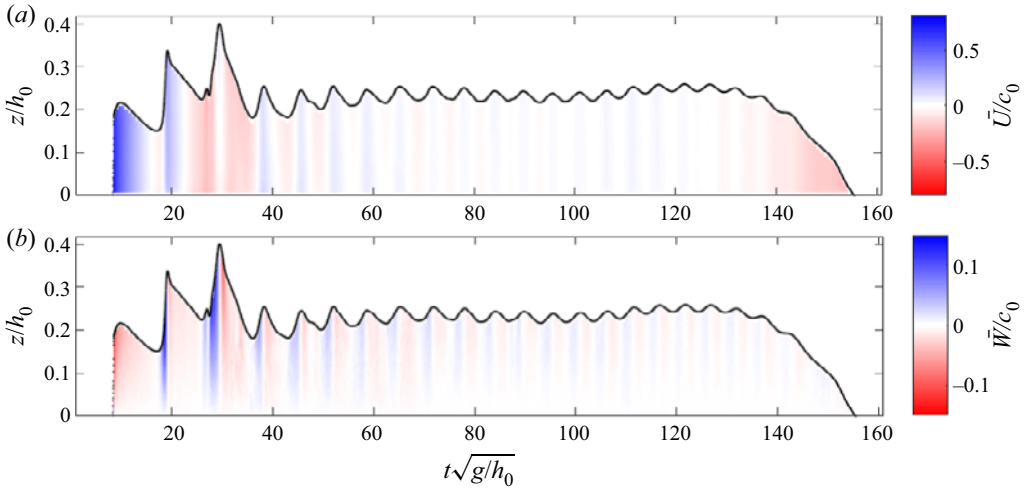


Figure 24. Time histories of UBs with  $F_{in} = 1.1$  free surface elevations and ensemble-averaged flow velocities in the water column at  $X = 2.26$  m. (a) Horizontal velocity component and (b) vertical velocity component.

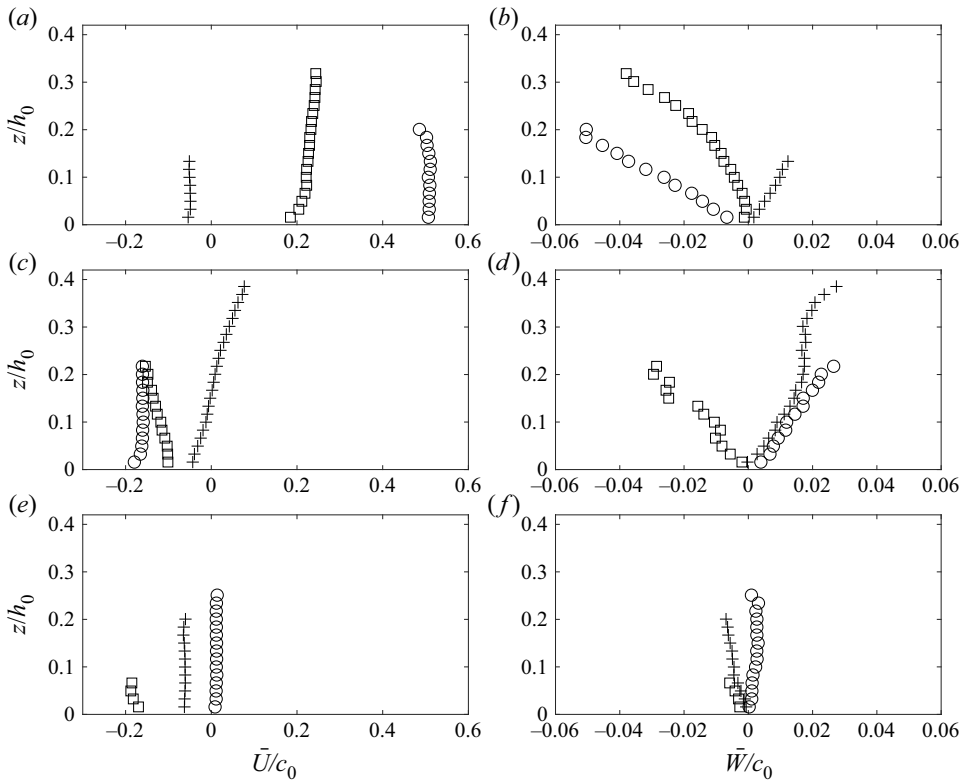


Figure 25. Vertical profiles of the ensemble-averaged flow velocities in the water column for the UB with  $F_{in} = 1.1$  at  $X = 2.26$  m. (a,c,e) Show the horizontal velocity component and (b,d,f) the vertical velocity component. (a,b)  $\circ$ :  $t\sqrt{g/h_0} = 9.64$ ;  $+$ :  $t\sqrt{g/h_0} = 17.49$ ;  $\square$ :  $t\sqrt{g/h_0} = 19.39$ . (c,d)  $\circ$ :  $t\sqrt{g/h_0} = 26.28$ ;  $+$ :  $t\sqrt{g/h_0} = 29.37$ ;  $\square$ :  $t\sqrt{g/h_0} = 33.79$ . (e,f)  $\circ$ :  $t\sqrt{g/h_0} = 126.40$ ;  $+$ :  $t\sqrt{g/h_0} = 139.21$ ;  $\square$ :  $t\sqrt{g/h_0} = 152.04$ .

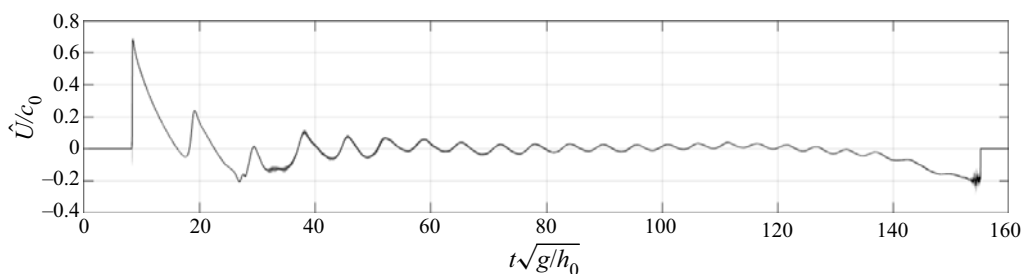


Figure 26. Time histories of dimensionless ensemble- and depth-averaged velocity of the UB with  $F_{in} = 1.1$  at  $X = 2.26$  m. Grey area represents one standard deviation from the ensemble-averaged values.

have linear profiles. The vertical velocity components appear to be much smaller than the horizontal velocity. Figures 25(c) and 25(d) show the velocity profiles in the vicinity of the third undulating crest ( $26.28 < t\sqrt{g/h_0} < 33.79$ ), which is also the maximum inundation depth. The horizontal velocities are always negative. However, near the crest the horizontal velocities become almost zero at the time the inundation depth reaches its maximum ( $t\sqrt{g/h_0} = 29.37$ ), having a small onshore velocity near the free surface and an offshore velocity close to the bottom boundary (in figure 25c). The horizontal flow velocities, measured before and after the maximum inundation stage, are almost uniform in the water column. As shown in figure 25(d) the vertical velocities are positive and almost linear in the water column before the maximum inundation depth. After the maximum inundation depth, the vertical velocities become negative with a linear profile. During the bore plateau ( $40 < t\sqrt{g/h_0} < 130$  in figure 24), both the free surface undulating heights and the horizontal velocities decrease. As indicated in figure 25(e) ( $t\sqrt{g/h_0} = 126.40$ ) at the end of the bore plateau the horizontal velocities are close to zero. As the bore recedes, the horizontal velocities turn into the offshore direction ( $t\sqrt{g/h_0} = 139.21$  and  $152.04$  in figure 25e). During the flooding the vertical velocities are very weak (figure 25f).

The ensemble- and depth-averaged flow velocities in the X-direction for the UB are plotted in figure 26. The averaged flow velocities register the maximum value at the arrival of the leading crest. The flow velocities decrease until the flow becomes almost quiescent, except for small oscillations with decreasing amplitudes. Near-zero flow velocities last during the flood plateau. Finally, the flow turns to the offshore direction during the bore rundown.

The time histories of the dimensionless fluctuating velocity components at FOV2 for the UB are plotted in figure 27. The profiles of the fluctuating velocity in the water column at different time instants are shown in figure 28. In this experiment, the first and second undulations did not break in the vicinity of FOV2, but the third undulation did. The fluctuating velocities associated with the breaking were captured by HSPIV. During the leading undulations (figure 28a,b) the fluctuating velocities are one order of magnitude smaller than the ensemble-averaged velocities. Afterward, fluctuating velocities increase during the backwash of the third undulation. At the time of the maximum inundation depth, horizontal fluctuating velocities are larger near the free surface and bottom boundary, while the vertical fluctuating velocities increase with water depths. Despite significant data scatter the magnitudes of the horizontal and vertical fluctuating velocity components are of the same order. During the flood plateau, the fluctuating velocities decrease and become almost zero near the end of the flood plateau (figure 28e,f).

The time history of the depth-averaged r.m.s. horizontal and vertical fluctuating velocities at  $X = 2.26$  m for the UB is plotted in figure 29. At the arrival of the undulating

Surf and swash flows generated by bores

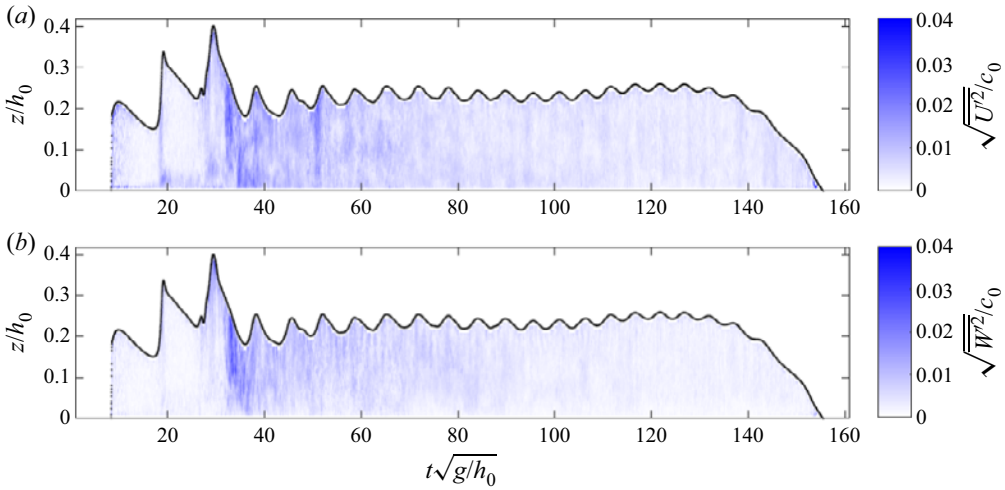


Figure 27. Time histories of free surface elevation and fluctuating velocity of the UB with  $F_{in} = 1.1$  in the water column at  $X = 2.26$  m. (a) The magnitude of horizontal velocity component and (b) the magnitude of vertical velocity component.

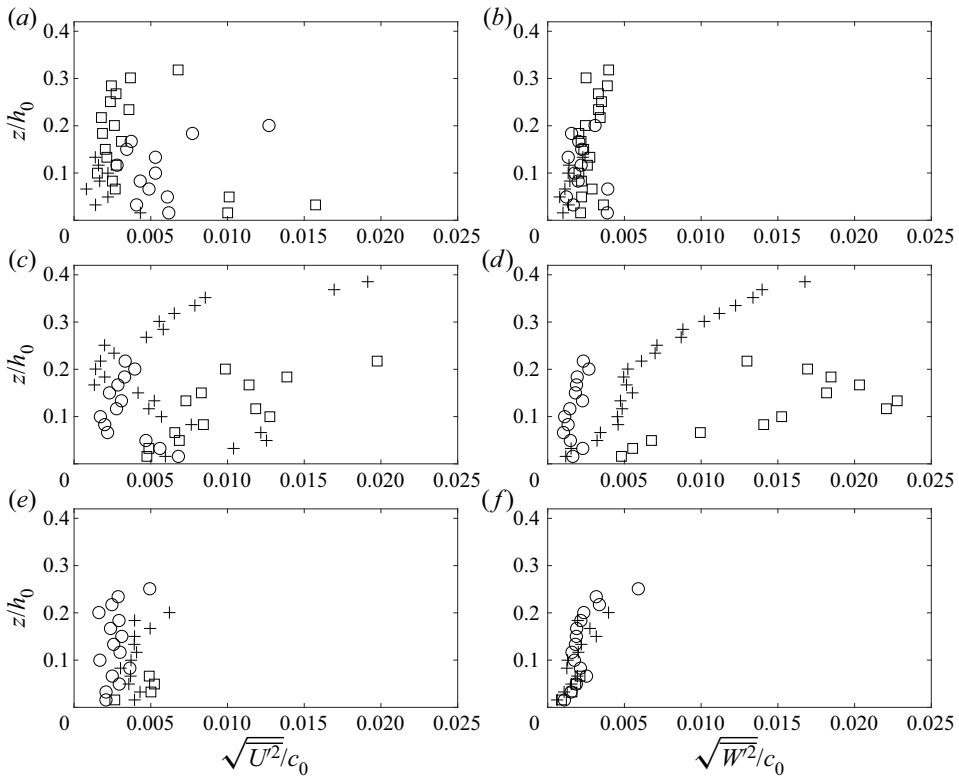


Figure 28. Vertical profiles of fluctuating velocity in the water column at  $X = 2.26$  m for the UB with  $F_{in} = 1.1$ . (a,c,e) Show the magnitude of horizontal velocity component and (b,d,f) display the magnitude of vertical velocity component. (a,b) ○:  $t\sqrt{g/h_0} = 9.64$ ; +:  $t\sqrt{g/h_0} = 17.49$ ; □:  $t\sqrt{g/h_0} = 19.39$ . (c,d) ○:  $t\sqrt{g/h_0} = 26.28$ ; +:  $t\sqrt{g/h_0} = 29.37$ ; □:  $t\sqrt{g/h_0} = 33.79$ . (e,f) ○:  $t\sqrt{g/h_0} = 126.40$ ; +:  $t\sqrt{g/h_0} = 139.21$ ; □:  $t\sqrt{g/h_0} = 152.04$ .

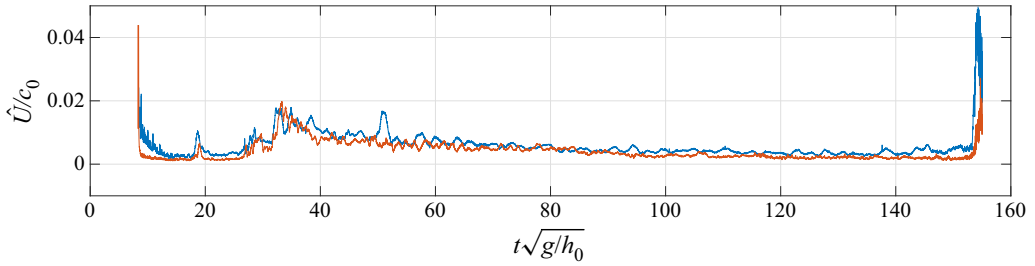


Figure 29. Time histories of the depth-averaged r.m.s. values of the fluctuating velocity at  $X = 2.26$  m. Here,  $F_{in} = 1.1$ . Blue line: magnitude of the horizontal velocity component; orange line: magnitude of the vertical velocity component.

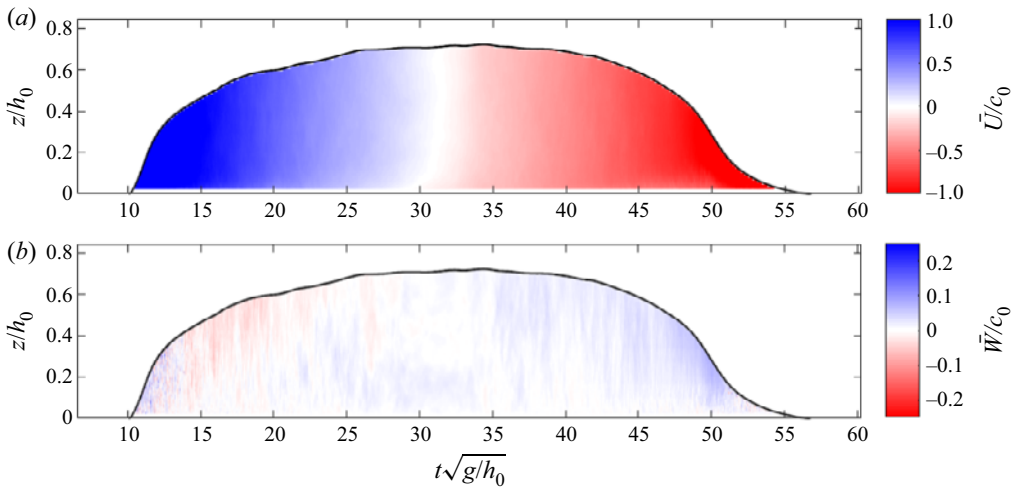


Figure 30. Time histories of free surface elevation and ensemble-averaged flow velocities in the water column at  $X = 2.26$  m for a BB with  $F_{in} = 1.6$ . (a) Horizontal velocity component and (b) vertical velocity component.

front and during the retreat phase, the magnitude of the fluctuating velocity is the largest. At those periods water depths are very shallow, therefore, larger noise readings are expected. The first significant increase in fluctuating velocity occurs at the arrival of the second undulation, but it is during the wave trough of the third undulation that the most significant increase in fluctuating velocity is observed. During the flood plateau the fluctuating velocity decreases steadily. Both horizontal and vertical fluctuating velocities show similar values during the entire event.

### 6.2. Breaking bore

For the BB the dimensionless ensemble-averaged horizontal and vertical velocity components at FOV2 are plotted in figure 30. The resolution for the BB HSPIV measurements at FOV2 is 2 mm and the FOV dimension is  $0.318 \times 0.168$  m. The maximum flow velocity measurable with this resolution is  $0.5 \text{ m s}^{-1}$ . Velocity profiles at different time instants are also shown in figure 31. Recall that velocity components at FOV2,  $U$  and  $W$ , are in the direction along the beach face and normal to it, respectively.

The overall pattern of the horizontal velocity is relatively simplistic. During the first half of the bore generated swash process the horizontal velocity is in the onshore direction,

Surf and swash flows generated by bores

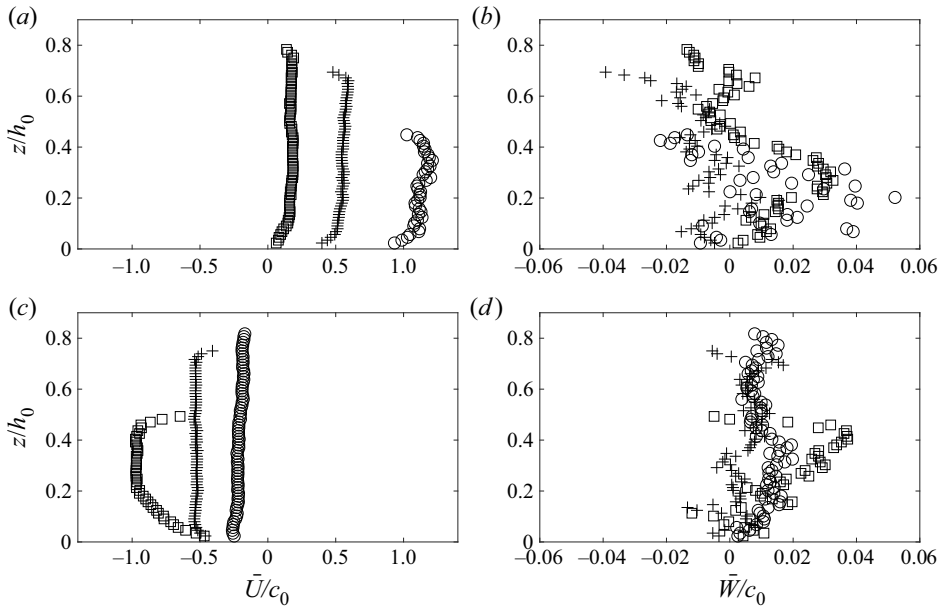


Figure 31. Vertical profiles of ensemble-averaged flow velocities in the water column at  $X = 2.26$  m during the BB with  $F_{in} = 1.6$ . (a,c) Show the magnitude of horizontal velocity component and (b,d) display the magnitude of vertical velocity component. (a,b)  $\circ$ :  $t\sqrt{g/h_0} = 12.82$ ;  $+$ :  $t\sqrt{g/h_0} = 20.25$ ;  $\square$ :  $t\sqrt{g/h_0} = 27.67$ . (c,d)  $\circ$ :  $t\sqrt{g/h_0} = 35.07$ ;  $+$ :  $t\sqrt{g/h_0} = 42.49$ ;  $\square$ :  $t\sqrt{g/h_0} = 49.87$ .

while it turns to the offshore direction during the second half of the bore duration (figure 30). Moreover, the velocity profiles are almost uniform in the water column. The magnitude of the vertical velocity is always much smaller than that of the horizontal velocity, making the flow more or less uni-directional. Negative velocities are dominant while the water depth increases and positive velocities are observed as the water retreats.

To demonstrate the details of the velocity pattern, the profiles of the horizontal and vertical velocities in the water column are plotted for  $12.82 < t\sqrt{g/h_0} < 27.67$ , during the bore front phase (figure 31a,b). Very close to the arrival time of the bore front,  $t\sqrt{g/h_0} = 12.82$ , the horizontal velocity quickly reaches its maximum value. As the water depth increases the velocities are reduced (i.e.  $t\sqrt{g/h_0} = 20.25$ ) until they become close to zero for a short period in the vicinity of the maximum depth (see  $t\sqrt{g/h_0} = 27.67$ ). During the runup flow process, the vertical velocities are small in comparison with the corresponding horizontal velocities. During the down-rush flow phase ( $35.07 < t\sqrt{g/h_0} < 49.87$ , figure 31c,d), the horizontal velocities are in the offshore direction with increasing magnitude and decreasing water depth. The vertical velocities are relatively small and do not show a clear structure. The ensemble- and depth-averaged flow velocities in the  $X$ -direction are plotted in figure 32. The flow velocity measurements show that the maximum velocity is reached instantaneously at the beginning of the swash flow. The averaged flow velocities decrease almost linearly until the end of the swash flows, when the maximum (negative) down-rush flow velocities are registered. Note that the swash flow pattern for the BB is quite different from that of the UB shown in figure 26, where a long flood period is a dominating feature.

The time histories of the dimensionless fluctuating velocity components at FOV2 for the BB are plotted in figure 33. The fluctuating velocity profiles in the water column

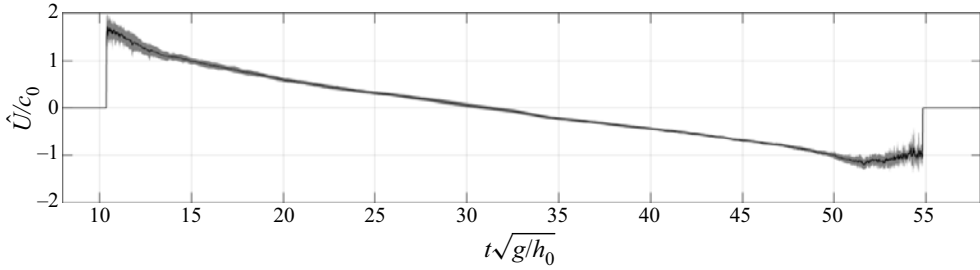


Figure 32. Time histories of dimensionless ensemble- and depth-averaged horizontal velocity at  $X = 2.26$  m measured from the HSPIV data for the BB with  $F_{in} = 1.6$ . Grey area represents one standard deviation from the average.

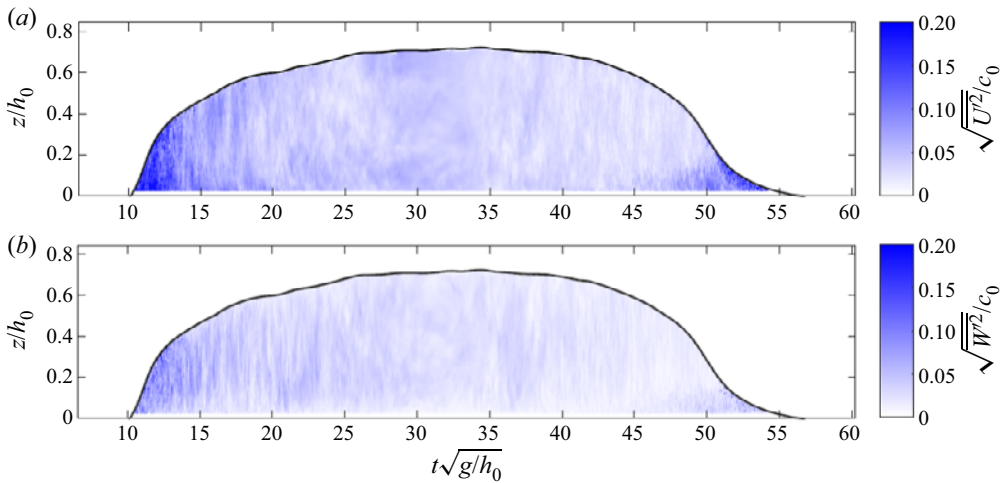


Figure 33. Time histories of free surface elevation and fluctuating velocities in the water column for the BB with  $F_{in} = 1.6$  at  $X = 2.26$  m. (a) The horizontal velocity component and (b) the vertical velocity component.

at different time instants are also shown in [figure 34](#). Overall, the magnitudes of the fluctuating velocity are more or less the same and they are one order of magnitude smaller than the ensemble-averaged horizontal velocity component, but are of the same order of magnitude as the ensemble-averaged vertical velocity. As shown in [figures 34\(a\)](#) and [34\(b\)](#), during the up-rush flow phase, ( $12.28 < t\sqrt{g/h_0} < 27.67$ ), the fluctuating velocities reach their maximum values at the initial stage of the bore arrival (i.e.  $t\sqrt{g/h_0} = 12.28$ ). The fluctuating velocities are later observed throughout the water column with a uniform profile (i.e.  $t\sqrt{g/h_0} = 20.25$  and  $27.67$ ). This feature persists during the down-rush flow phase (i.e.  $t\sqrt{g/h_0} = 35.07$  and  $42.49$ ), as shown in [figures 34\(c\)](#) and [34\(d\)](#). At  $t\sqrt{g/h_0} = 49.87$ , the down-rush velocity becomes strong and fluctuating velocities are captured near the bottom boundary.

The time history of the r.m.s. values of the depth-averaged horizontal and vertical fluctuating velocities at  $X = 2.26$  m for the BB are plotted in [figure 35](#). The horizontal velocity is largest at the bore arrival and the bore retreat period. The horizontal velocities are nearly twice the observed values during the bore front at FOV1 in [figure 23](#).

In contrast to the data for constant depth, in which the fluctuating velocities are mostly present in the vicinity of the bore front with relatively low magnitude below the free surface, during the bore arrival at the slope the fluctuating velocities appear in the entire

## Surf and swash flows generated by bores

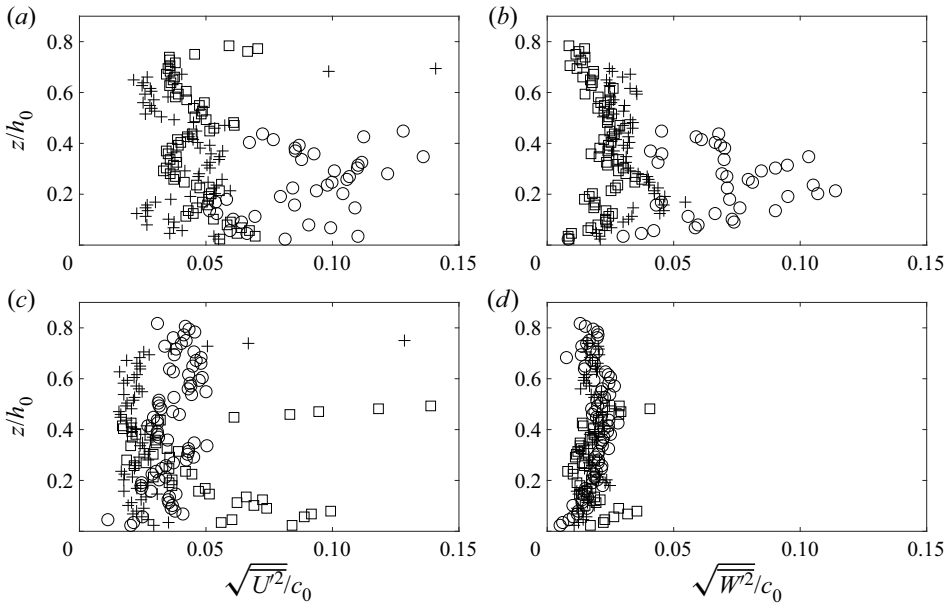


Figure 34. Vertical profiles of the fluctuating velocities in the water column at  $X = 2.26$  m during the bore front. Here,  $F_{in} = 1.6$ . (a,b) Show the magnitude of the horizontal velocity and (c,d) the magnitude of the vertical velocity. (a,b)  $\circ$ :  $t\sqrt{g/h_0} = 12.82$ ;  $+$ :  $t\sqrt{g/h_0} = 20.25$ ;  $\square$ :  $t\sqrt{g/h_0} = 27.67$ . (c,d)  $\circ$ :  $t\sqrt{g/h_0} = 35.07$ ;  $+$ :  $t\sqrt{g/h_0} = 42.49$ ;  $\square$ :  $t\sqrt{g/h_0} = 49.87$ .

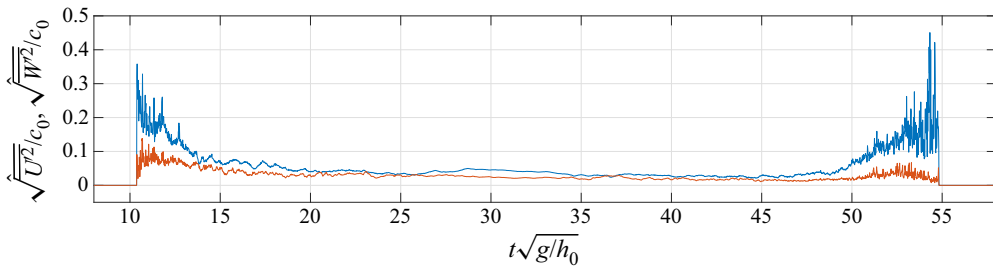


Figure 35. Time histories of the r.m.s. values of the depth-averaged fluctuating velocity at  $X = 2.26$  m. Here,  $F_{in} = 1.6$ . Blue line: the horizontal component; orange line: the vertical component.

water column similar to those observed at the bore front in constant depth. At the very end of the bore backwash water depths become extremely shallow and larger noise readings are expected due to the short distance to both the bottom and free surface boundaries, similar to what was observed during the UB swash, and ripples on the free surface.

In between the bore runup and rundown the horizontal and vertical fluctuating velocities are similar and decrease with time. The fluctuating velocities during this period are similar to those observed during the bore plateau and bore tail at FOV1.

## 7. Concluding remarks

Using a long-stroke wavemaker, undulating and breaking bores with different strengths and lengths are generated in a wave flume. Both non-decaying and decaying bores

are investigated. Bore strengths, heights and lengths are compared with those calculated from the method of characteristics, with excellent agreement.

The swash flow characteristics, including the maximum inundation depth,  $I$ , maximum runup height,  $R$ , and flood duration,  $T_f$ , are measured and analysed. These data are used to check the predictive formulas presented in Barranco & Liu (2021). The comparisons demonstrate that these predictive formulas are also reasonably accurate for the non-decaying bores. This further confirms the hypothesis that bore-induced swash flows can be described by the bore characteristics measured at the beach toe and the beach slope, being independent of the bore generation mechanism.

Moreover, for decaying bores the maximum inundation depth data can be estimated using the predictive formulas with  $L_b = 0$ . Since the runup heights are unaffected by the length of the bores, the same formula presented in Barranco & Liu (2021) can be applied to decaying bores. However, the runup results point out that the bore length at the beach toe and the slope may have a small influence on the maximum runup height for very short and decaying bores. This influence is expected to increase for a milder slope, in which the bore propagates a longer distance on the slope before reaching the shoreline.

Using a HSPIV system, ensemble-averaged flow velocities and fluctuating velocities under an UB and a BB are measured in both a constant water depth region and in the vicinity of the shoreline. To the best of our knowledge, this is the first comprehensive set of swash flow velocity measurements associated with both UB and BB bores in the literature.

For the UB in constant depth, the velocity profiles under the first three undulations, which have descending wave heights, are compared with those under three solitary waves with matching wave heights. Excellent agreement is observed. These observations provide further evidence on the similarity between UBs and a train of rank-ordered solitons (El 2007; Grimshaw *et al.* 2007; Brühl *et al.* 2022).

The bore-induced swash flow with the presence of a relatively long flooding phase is captured in the present measurements for the first time. This flooding phase has the potential to prompt sediment deposition during the swash event. Moreover, it separates the rundown flow produced by the bore retreat from the swash flows produced by the leading undulations. This makes the rundown during the bore retreat phase only dependent on the bore tail, contrary to the observation by Pujara *et al.* (2020).

For the BB case, the depth-averaged horizontal flow velocities in the constant water depth region agree well with those predicted by the bore relations, based on the method of characteristics. However, while the bore relations assume constant flow velocity profile in the water column, the observed flow velocities are larger near the free surface and smaller in the region below the initial water depth, similar to the profiles observed under BBs generated by dam-break systems (Hornung *et al.* 1995). For the BB in constant water depth, fluctuating velocities are strongest near the breaking front. Fluctuating velocities are also observed in the entire water column during the bore plateau and bore tail.

**Supplementary material and movies.** Supplementary material and movies are available at <https://doi.org/10.1017/jfm.2023.116>.

**Funding.** P.L.-F.L. would like to acknowledge the support from the National University of Singapore, Cornell University, and the Ministry of Education in Singapore through a research grant (MOE2018-T2-2-040). This research was also supported in part by the Yushan Program of the Ministry of Education in Taiwan. I.B. would like to thank the Ministry of Education in Singapore for a PhD scholarship. Insightful discussions with H. Yeh and I.M. Sou are also appreciated.

**Declaration of interests.** The authors report no conflict of interest.

**Author ORCIDs.**

 Ignacio Barranco <https://orcid.org/0000-0001-6506-7626>;

 Philip L.-F. Liu <https://orcid.org/0000-0002-2170-5507>.

**Author contributions.** I.B.: analytical analysis; conducting experiment; data analysis; writing. P.L.-F.L.: conceptualization; writing – review and editing; supervision; project administration.

**Appendix A. Wavemaker generated bore in constant depth**

As explained in Barranco & Liu (2021), it is desirable to predict the swash flow characteristics based on the bore strength and the bore length at the beach toe. Barranco & Liu extended the work by Hogg (2006) and Goater & Hogg (2011) and provided analytical solutions to calculate the bore duration and bore length of a bore generated by a dam-break system with different reservoir lengths. A similar analysis is presented here to describe the evolution of a bore generated with a piston-type wavemaker moving with a constant velocity.

Consider a uniform bore generated by a piston wavemaker that accelerates instantaneously, moves with a constant velocity, travels a distance  $L_p$  and stops suddenly (figure 36). At the moment of stoppage, a fan of positive characteristics with constant  $\beta$  values departs from the paddle position on the characteristic plane, forming the bore tail. The front of the tail coincides with the end of bore plateau and will propagate with velocity  $u_b + c_b$  (see figure 36b). The last characteristic of the bore tail determines the final water depth in front of the paddle ( $h_f = c_f^2/g$ ), where  $c_f - u_f/2 = c_b - u_b/2$  from the Riemann invariant  $\beta$  relation and  $u_f = 0$ .

The effective period of a bore ( $T_{bt}$ ) is defined as the time interval between the bore front arrival time ( $t_{arr}$ ) and the arrival of the beginning of the bore tail at the same location ( $t_{end}$ )

$$T_{bt} = t_{end} - t_{arr}. \tag{A1}$$

The arrival times of the bore front and the beginning of the bore tail at a distance  $x_t > 0$  from the final position of the wavemaker can be calculated as

$$t_{arr} = (L_p + x_t)/U_b, \tag{A2}$$

$$t_{end} = t_g + (x_t)/(u_b + c_b), \tag{A3}$$

where  $t_g$  is the duration for which the wavemaker moves with constant velocity (see figure 36)

$$t_g = L_p/u_b. \tag{A4}$$

Substituting (A2), (A3) and (A4) into (A1), the effective period of a bore at a given location,  $x_t$ , is

$$T_{bt} = \frac{L_p}{u_b} + \frac{x_t}{u_b + c_b} - \frac{L_p + x_t}{U_b}, \tag{A5}$$

where  $U_b$ ,  $u_b$  and  $c_b$  can be calculated as a function of  $F_{in}$  and  $c_0$  by using (3.1), (3.2) and (3.3), respectively.

The initial length of a bore ( $L_{b0}$ ) is defined as the distance from the bore front location to the final position of the wavemaker at the moment when the wavemaker stops (see figure 36). Thus, the initial length of a bore can be calculated in terms of the bore

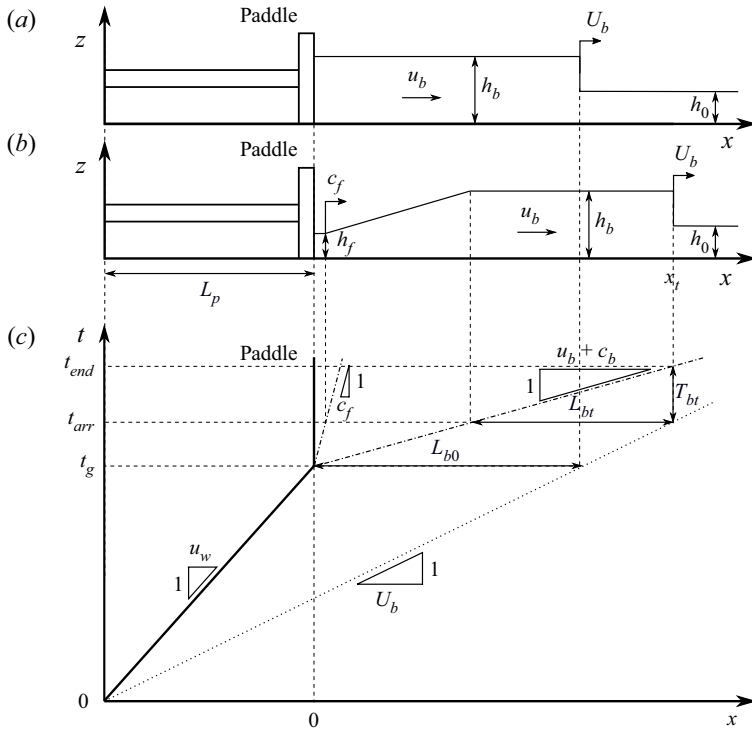


Figure 36. Panels (a,b) show the two-dimensional vertical representations of the generated bore at times  $t_g$  and  $t_{arr}$ , respectively. Panel (c) shows a sketch of the characteristic plane of a bore generated by a piston wavemaker moving with velocity  $u_b$  for a distance  $L_p$ . The solid line represents the wavemaker displacement, the dotted line the bore front propagation and dashed-dotted lines positive characteristics departing from the wavemaker at the time of stoppage (the tail begins and ends with velocities  $u_b + c_b$  and  $c_f$ , respectively).

propagation speed, the wavemaker speed and the wavemaker stroke

$$L_{b0} = U_b \frac{L_p}{u_b} - L_p. \tag{A6}$$

Using (3.2) the initial bore length can be written as a function of the bore strength and wavemaker stroke

$$\frac{L_{b0}}{L_p} = \frac{\sqrt{1 + 8F_{in}^2} - 1}{\sqrt{1 + 8F_{in}^2} - 3} - 1. \tag{A7}$$

Since the beginning of the bore tail propagates faster than the bore front does, the effective bore length decreases as the bore propagates away from the wave paddle (see figure 36). The effective bore length at the beach toe,  $L_b$ , which is located at a distance  $x_t = L_f$  from the final position of the wave paddle, can be calculated as the distance  $L_f$  minus the location of the beginning of the bore tail when the bore reaches the beach toe ( $t_{ioe}$ )

$$L_b = L_f - (t_{ioe} - t_g)(u_b + c_b), \tag{A8}$$

## Surf and swash flows generated by bores

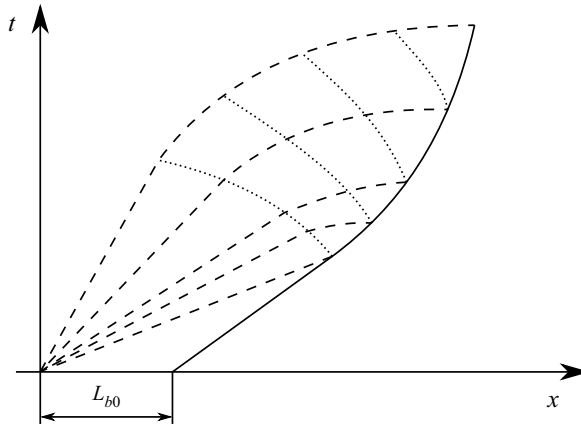


Figure 37. Decaying bore characteristics. The continuous line represents the bore front, dashed lines the positive characteristics with origin at the paddle's final position and dotted lines the negative characteristics with their origin at the bore front.

where  $t_{toe}$  and  $t_g$  can be calculated by (A2) and (A4), respectively. By substituting these variables into (A8) the effective bore length at the beach toe can be calculated as

$$L_b = L_f \left( 1 - \frac{u_b + c_b}{F_{in} c_0} \right) + L_p \left( \frac{u_b + c_b}{c_0} \right) \left( \frac{c_0}{u_b} - \frac{1}{F_{in}} \right). \quad (\text{A9})$$

### Appendix B. Decaying bore

To evaluate the decay rate of a bore, numerical solutions based on the method of characteristics (Lax 1948) are obtained. While the wavemaker piston moves with constant velocity, positive characteristics depart from the paddle with constant  $u_b$  and  $c_b$  values, which can be calculated as functions of the input bore strength  $F_{in}$  using (3.2) and (3.3), respectively. When the paddle stops, a fan of characteristics departs from the paddle location, forming the bore tail, in which the flow velocities and depths follow  $\beta = 2c - u = 2c_b - u_b = \text{constant}$ . This region is delimited by the beginning of the bore tail, in which  $u = u_b$  and  $c = c_b$ , and the undisturbed water in front of the paddle following the bore tail, in which  $u = 0$  and  $c = c_b - 1/2u_b$ . The instant the tail of the bore reaches the bore front, the flow mass and momentum behind the front start to decrease, reducing the strength of the bore. Lax (1948) provides a numerical solution to solve the decay of a bore given its initial strength ( $F_{in}$ ) and length ( $L_{b0}$ ) at the time of paddle stoppage (see figure 37). The method propagates the positive characteristics (bore tail) until they reach the bore front. When the bore tail characteristics reach the bore front the strength of the bore is reduced and negative characteristics depart from the bore front. These negative characteristics eventually modify the velocities and water depths of the subsequent positive characteristics reaching the bore front.

The Lax method is used to track the bore front location and its strength for all the decaying laboratory experiments. For each  $F_{in}$  and  $L_p$ ,  $L_{b0}$  is calculated by employing (A7). The positive characteristics departing from the paddle have equidistant  $u$  values from  $u = u_b$  to  $u = 0$  and  $c$  values are calculated using  $c = c_b - (u_b - u)/2$ . The convergence of the method is analysed for the case  $L_p/h_0 = 13.33$ , and it is tested for the range of bore strengths which reach the beach toe as decaying bores ( $F_{in} > 1.34$ ). The convergence criterion is  $|t_{toe}(n+1) - t_{toe}(n)|/t_{toe}(n+1) < 0.001$ , where  $t_{toe}$  is the arrival time of

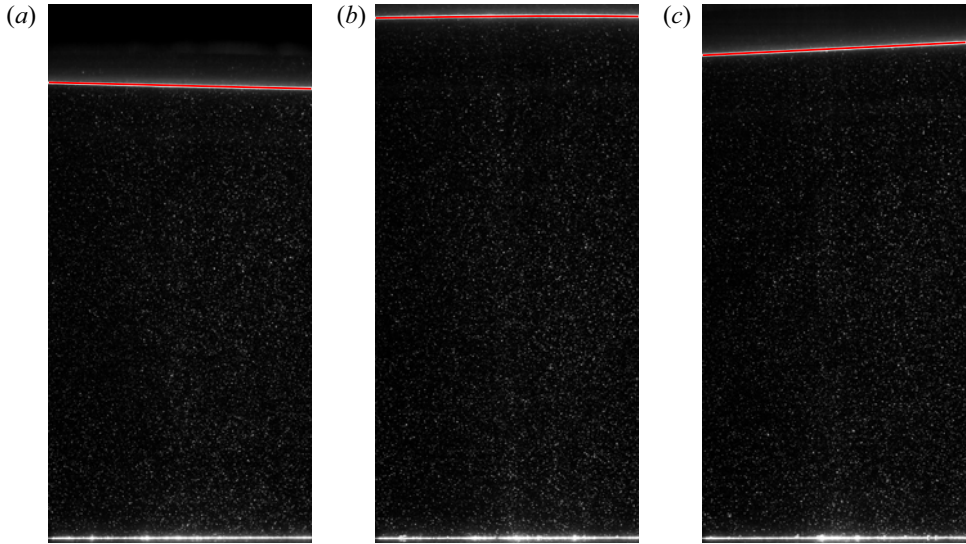


Figure 38. The HSPIV images of the UB at FOV1. The identified free surface is given by red line:  
 (a)  $t\sqrt{g/h_0} = -42.15$ ; (b)  $t\sqrt{g/h_0} = -38.27$ ; (c)  $t\sqrt{g/h_0} = -36.47$ .

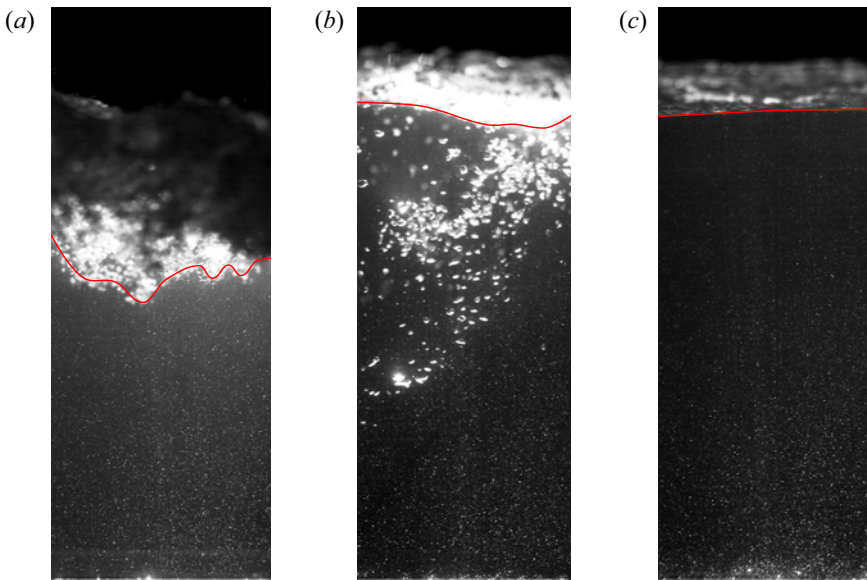


Figure 39. The HSPIV images of the BB at FOV1. The identified free surface is given by red line:  
 (a)  $t\sqrt{g/h_0} = -37.12$ ; (b)  $t\sqrt{g/h_0} = -33.73$ ; (c)  $t\sqrt{g/h_0} = -28.20$ .

the bore front at the beach toe and  $n$  is the number of characteristics. The number of characteristics in the simulations varies from 100 to 10000 with 100 characteristic intervals. The most restrictive case is  $F_{in} = 1.8$  for which the results converge for 3400 characteristics.

This method is employed to calculate the strength of the decaying bores reaching the capacitance gauges in the laboratory experiments. For each wavemaker stroke the bore

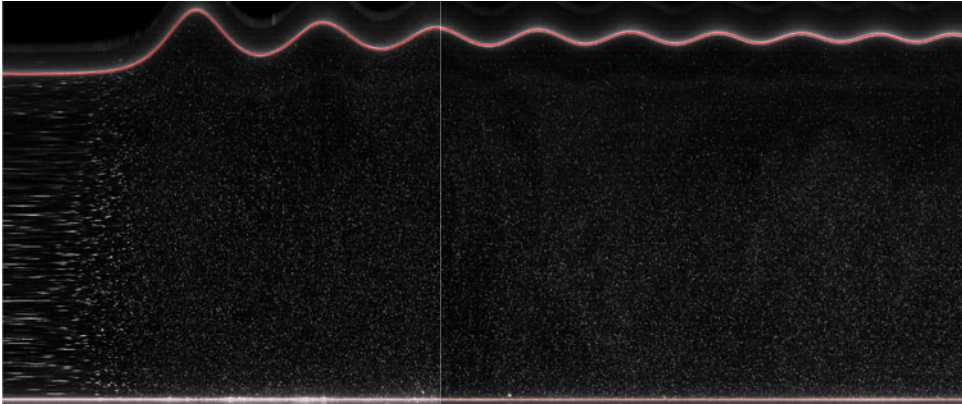


Figure 40. Timestack image at FOV1 centre from HSPIV images for UB. Identified free surface and bottom boundary in red.

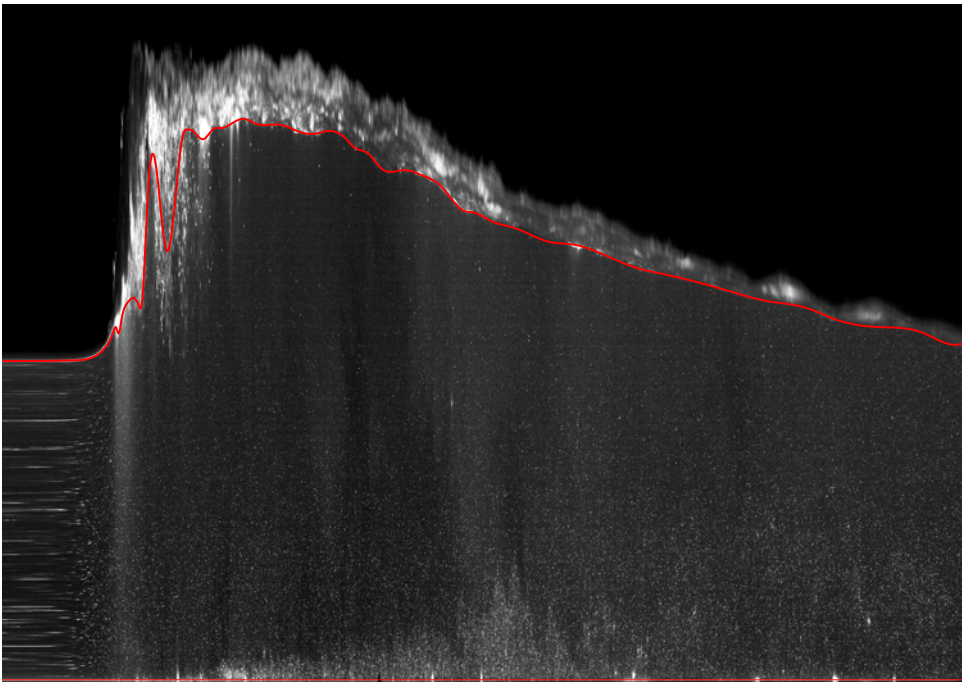


Figure 41. Timestack image at FOV1 centre from HSPIV images for BB. Identified free surface and bottom boundary in red.

decay is calculated for a range of input bore strengths  $F_{in} = 1.05$  to  $F_{in} = 2$  with a 0.01 interval. For each simulation 4000 characteristics are employed. The results are plotted in [figure 5](#), in which  $F_{34}$  and  $F_{56}$  are the mean of the bore strengths at CG3 and CG4 and at CG5 and CG6, respectively. None of the cases analysed are predicted to be decaying at CG1 and CG2.

### **Appendix C. The HSPIV free surface identification**

During the HSPIV experiments, the free surface is identified manually in space (every 200 frames) and in time (every 200 pixels). The free surface for the UB is easily identified

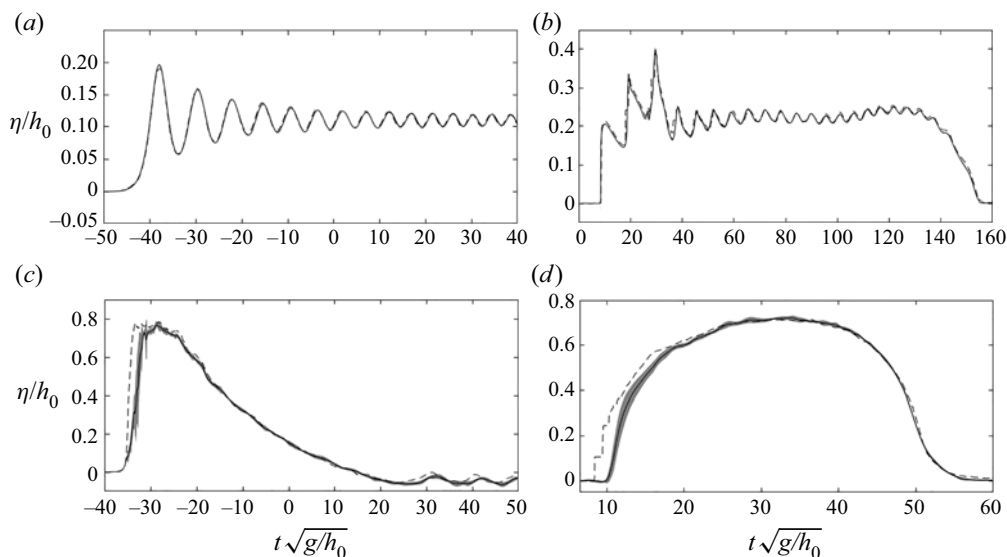


Figure 42. Time histories of dimensionless free surface measured from the HSPIV data, solid line, and at capacitance gauges, dashed line. Grey area represents the HSPIV measurements plus–minus one standard deviation. The UB measurements are in panels (a,b), and BB measurements in panels (c,d). Measurements at  $x = -9.87$  m (FOV1) in the left panels, and measurements at  $x = 2.28$  m (FOV2) in the right panels.

(see figure 38). For the BB case the free surface is identified as the lower boundary of the aerated flow region (figure 39a). However, bubbles inside the water body are visible and will affect the velocity measurements (figure 39b). In addition to the free surface identification at given frames, the free surface is also identified in time at target locations. For this purpose, image sequences, or timestacks, formed by consecutive columns of pixels taken from consecutive frames at the target location are assembled (figures 40 and 41). The missing free surface data are interpolated in time and space.

For each case and FOV, the ensemble-averaged free surface is calculated. The free surfaces measured from the HSPIV data and the measurements at the CG2 (configuration 3) and US3 (configuration 2) are plotted in figure 42. The agreement for the UB is remarkable at both FOV1 and FOV2. In the BB case it is observed that the capacitance gauge measures larger heights on the BB front, compared with the HSPIV measurements. This difference represents the aerated flow in the breaking front, which has been neglected in the HSPIV measurements (see figure 41).

#### REFERENCES

- BARNES, M. & BALDOCK, T. 2006 Bed shear stress measurements in dam break and swash flows. In *Proceedings of the International Conference on Civil and Environmental Engineering (ICCEE-2006)*, The University of Hiroshima, Higashihiroshima, Japan. ICCEE.
- BARNES, M.P., O'DONOGHUE, T., ALSINA, J.M. & BALDOCK, T.E. 2009 Direct bed shear stress measurements in bore-driven swash. *Coast. Engng* **56** (8), 853–867.
- BARRANCO, I. 2021 Generation and propagation of tsunami-like bores and characteristics of the produced inundation. PhD thesis, National University of Singapore.
- BARRANCO, I. & LIU, P.L.-F. 2021 Run-up and inundation generated by non-decaying dam-break bores on a planar beach. *J. Fluid Mech.* **915**, A81.
- BRÜHL, M., PRINS, P.J., UJVARY, S., BARRANCO, I., WAHLS, S. & LIU, P.L.-F. 2022 Comparative analysis of bore propagation over long distances using conventional linear and KdV-based nonlinear Fourier transform. *Wave Motion* **111**, 102905.

## Surf and swash flows generated by bores

- CHANSON, H. 2011 Current knowledge in tidal bores and their environmental, ecological and cultural impacts. *Environ. Fluid Mech.* **11** (1), 77–98.
- EL, G.A. 2007 Korteweg–de Vries Equation: Solitons and Undular Bores. In *WIT Transactions on State-of-the-art in Science and Engineering*, vol. 9. WIT.
- GOATER, A.J.N. & HOGG, A.J. 2011 Bounded dam-break flows with tailwaters. *J. Fluid Mech.* **686**, 160–186.
- GRIMSHAW, R. 1970 The solitary wave in water of variable depth. *J. Fluid Mech.* **42** (3), 639–656.
- GRIMSHAW, R.H.J., ZHANG, D.-H. & CHOW, K.W. 2007 Generation of solitary waves by transcritical flow over a step. *J. Fluid Mech.* **587**, 235–254.
- HOGG, A.J. 2006 Lock-release gravity currents and dam-break flows. *J. Fluid Mech.* **569**, 61–87.
- HORNUNG, H.G., WILLERT, C. & TURNER, S. 1995 The flow field downstream of a hydraulic jump. *J. Fluid Mech.* **287**, 299–316.
- KIKKERT, G.A., O'DONOGHUE, T., POKRAJAC, D. & DODD, N. 2012 Experimental study of bore-driven swash hydrodynamics on impermeable rough slopes. *Coast. Engng* **60**, 149–166.
- LAX, A. 1948 Decaying shocks, a comparison of an approximate analytic solution with a finite difference method. *Commun. Pure Appl. Maths* **1** (3), 247–257.
- LIGGETT, J.A. 1994 *Fluid Mechanics*. McGraw-Hill.
- LIN, C., KAO, M.-J., WONG, W.-Y., SHAO, Y.-P., HU, C.-F., YUAN, J.-M. & RAIKAR, R.V. 2019 Effect of leading waves on velocity distribution of undular bore traveling over sloping bottom. *Eur. J. Mech. (B/Fluids)* **73**, 75–99.
- LIN, C., KAO, M.-J., YUAN, J.-M., RAIKAR, R.V., HSIEH, S.-C., CHUANG, P.-Y., SYU, J.-M. & PAN, W.-C. 2020a Similarities in the free-surface elevations and horizontal velocities of undular bores propagating over a horizontal bed. *Phys. Fluids* **32** (6), 063605.
- LIN, C., KAO, M.-J., YUAN, J.-M., RAIKAR, R.V., WONG, W.-Y., YANG, J. & YANG, R.-Y. 2020b Features of the flow velocity and pressure gradient of an undular bore on a horizontal bed. *Phys. Fluids* **32** (4), 043603.
- MILLER, R.L. 1968 Experimental determination of run-up of undular and fully developed bores. *J. Geophys. Res.* **73** (14), 4497–4510.
- O'DONOGHUE, T., POKRAJAC, D. & HONDEBRINK, L.J. 2010 Laboratory and numerical study of dambreak-generated swash on impermeable slopes. *Coast. Engng* **57** (5), 513–530.
- PUJARA, N., MILLER, D., PARK, Y.S., BALDOCK, T.E. & LIU, P.L.-F. 2020 The influence of wave acceleration and volume on the swash flow driven by breaking waves of elevation. *Coast. Engng* **158**, 103697.
- SHUTO, N. 1985 The Nihonkai-Chubu earthquake tsunami on the North Akita Coast. *Coast. Engng Japan* **28** (1), 255–264.
- SIMPSON, J.H., FISHER, N.R. & WILES, P. 2004 Reynolds stress and TKE production in an estuary with a tidal bore. *Estuar. Coast. Shelf Sci.* **60** (4), 619–627.
- STANSBY, P.K., CHEGINI, A. & BARNES, T.C.D. 1998 The initial stages of dam-break flow. *J. Fluid Mech.* **374**, 407–424.
- STOKER, J.J. 1957 *Water Waves, The Mathematical Theory with Application*. Interscience.
- TAKAHASHI, K. & TOMITA, T. 2013 Simulation of the 2011 tohoku tsunami in Kuji Bay using three-dimensional non-hydrostatic numerical model. *J. Japan Soc. Civ. Engrs* **69** (2), 166–170.
- THIELICKE, W. & STAMHUIS, E.J. 2014 Pivlab-towards user-friendly, affordable and accurate digital particle image velocimetry in matlab. *J. Open Res. Softw.* **2** (1), e30.
- WESTERWEEL, J. & SCARANO, F. 2005 Universal outlier detection for PIV data. *Exp. Fluids* **39** (6), 1096–1100.
- YEH, H.H., GHAZALI, A. & MARTON, I. 1989 Experimental study of bore run-up. *J. Fluid Mech.* **206**, 563–578.